SAND2018-9167R

U.S. DEPARTMENT OF ENERGY

SAND 2018-XXXX

Sandia National Laboratories

COMPARISON OF HEAT FLUX PREDICTIONS OVER THE BLOTTNER CYLINDER AND SPHERE

BENJAMIN COUCHMAN*

Abstract. The prediction of heat flux over a sphere in hypersonic flow is an interesting and challenging problem. When using solutions to the Navier-Stokes equations to predict the heat flux, a common source of numerical error is a phenomenon known as 'grid imprinting'. Rather than the axisymmetric heat flux profile expected for a spherical surface, the topology of the grid can be seen in the surface heat flux distribution. We will examine the origin of this phenomenon; specifically the regions of the grid that contribute most. Comparisons will be made between second order finite volume and Discontinuous Galerkin (DG) results – the DG results will range from 2^{nd} to 4^{th} order. The Dual Weighted Residual (DWR) framework is used to obtain local error estimates for the heat flux integrated over the surface with respect to the grid for the DG results.

1. Introduction. A common source of numerical error in the prediction of heat fluxes using solutions to the Navier-Stokes equations over spheres in high-speed flows is a phenomenon described as grid imprinting. Rather than the axisymmetric heat flux profile expected for a spherical surface, the topology of the grid can be seen in the heat flux prediction, as shown in Figure 1.1, a similar feature is found in the results for Kirk et al. [7].

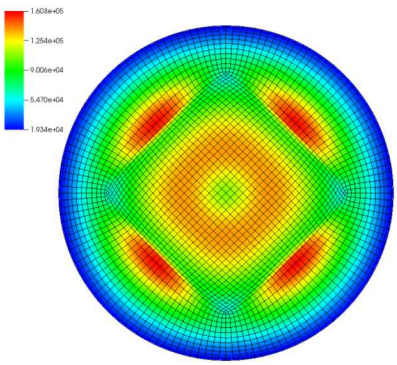

Fig. 1.1: Heat flux over the Blottner Sphere

In this paper we will investigate the origin of the grid imprinting phenomenon; specifically, in which regions of the computational domain does the grid topology effect the heat flux on the surface of the sphere. We examine the origin of these errors using Discontinuous Galerkin (DG) solutions to the Navier-Stokes equations, and the Dual-Weighted Residual (DWR) error estimation. This allows us to determine which regions of the computational domain are contributing most to the error in heat flux. The DG results are obtained using the Solution Adaptive Numerical Solver (SANS) from MIT. The finite volume results are obtained using Sandia Parallel Aerosciences Research Code (SPARC).

*Massachusetts Institute of Technology, blsc@mit.edu

We intend to answer the following research questions:

- Can we get good quality high-order heat fluxes on cylinders and spheres?
- Can we use features of the numerical solution to understand the error sources?
- What is the origin of this grid imprinting?

1.1. Mathematical Model. We solve the steady Navier-Stokes equations in conservation form, as given in Equation 1.1,

$$\nabla \cdot \mathbf{F}(u) - \nabla \cdot \mathbf{F}_v(u, \nabla u) = 0, \tag{1.1}$$

where,

$$\mathbf{F}(u) = \begin{bmatrix} \rho\mathbf{V} \\ \rho\mathbf{V}\mathbf{V} + p\mathcal{I} \\ \rho\mathbf{V}H \end{bmatrix} \quad \mathbf{F}_v(u, \nabla u) = \begin{bmatrix} 0 \\ \tau \\ q + p\mathbf{V} + \tau\mathbf{V} \end{bmatrix}. \tag{1.2}$$

Where ρ is the density, $\mathbf{V}$ is the velocity, p is the pressure, H is the total enthalpy, $q = k\nabla T$ is the heat flux, $\tau = \mu\left[\left(\nabla\mathbf{V} + (\nabla\mathbf{V})^T\right) - \frac{2}{3}(\nabla \cdot \mathbf{V})\mathcal{I}\right]$ is the viscous shear stress tensor, k is the Thermal conductivity, and μ is the viscosity.

These equations are closed under the assumption that the gas is calorificially perfect air with a gas constant (R) of $287 J/kg/K$ and a ratio of specific heats (γ) of 1.4. The viscosity is obtained using Sutherland's Law as reported by Blottner[4],

$$\mu = 1.458 \times 10^{-6} \frac{T^{1.5}}{T + 110.4} \tag{1.3}$$

where the temperature is in Kelvin, and the viscosity is in Pa. s. The thermal conducitity is determined assuming a constant Prandtl number of 0.72[4].

1.2. Numerical Method. The DG discretization finds a solution to the weak form of the Navier-Stokes equation in the space $\mathcal{W}_{h,p} = \left\{w \in L^2(\Omega) \,:\, w|_k \in P^p, \forall k \in \mathcal{T}_h\right\}$. This is the space of p^{th} order polynomials on each element of $\mathcal{T}_h$, which is the triangulation of the domain Ω. This corresponds solving,

$$R_{h,p}(u_{h,p}, w_{h,p}) = 0 \quad \forall w_{h,p} \in \mathcal{W}_{h,p}, \tag{1.4}$$

the semi-linear weighted residual, which is defined as,

$$R_{h,p}(u_{h,p}, w_{h,p}) = R^{adv}_{h,p}(u_{h,p}, w_{h,p}) + R^{visc}_{h,p}(u_{h,p}, w_{h,p}) + R^{source}_{h,p}(u_{h,p}, w_{h,p}). \tag{1.5}$$

Note that while the Navier-Stokes equations do not have a source term, an additional PDE to drive the artificial viscosity will be added to the system. This additional equation does contain a source term, which requires discretization.

We will make use of the following notation,

$$\{v\} = \frac{1}{2}\left(v^+ + v^-\right) \quad [\![v]\!] = v^+ n^+ + v^- n^-, \tag{1.6}$$

if v is a scalar, and,

$$\{v\} = \frac{1}{2}\left(v^+ + v^-\right) \quad [\![v]\!] = v^+ \cdot n^+ + v^- \cdot n^-, \tag{1.7}$$

if v is a vector. The terms $(v)^-$ and $(v)^+$ are the values of v evaluated from either side of a face.

The DG discretization of the advective term is given by,

$$R_{h,p}^{adv}(u,w) = \sum_{k\in\mathcal{T}_h}\int_{\Omega_k} -(\nabla w)^T\cdot\mathbf{F}(u)\,d\Omega + \sum_{f\in\Gamma_I}\int_f \left(w^+-w^-\right)^T\cdot\mathbf{H}\left(u^+,u^-,\mathbf{n}\right)\,d\Gamma + \sum_{f\in\Gamma_B}\int_f w^T\cdot\mathbf{H}^B\left(u^+,u^B,\mathbf{n}\right)\,d\Gamma, \quad (1.8)$$

where Γ_I is the set of interior faces, Γ_B is the set of boundary faces, $\mathbf{H}$ is the approximate Riemann flux of Roe, using Harten's entropy fix, and $\mathbf{H^B}$ is a numerical flux function on the boundary faces used to enforce the boundary conditions.

We define the viscous flux as $F_{visc}(u,\nabla u)\equiv\mathcal{A}(u)\nabla u$, which allows the DG discretization of the viscous terms using the BR2 method [2],

$$\begin{aligned}R_{h,p}^{visc}(u,w) = &\sum_{k\in\mathcal{T}_h}\int_{\Omega_k}(\nabla w)^T\cdot\mathcal{A}(u)\nabla u\,d\Omega\\ &+\sum_{f\in\Gamma_I}\int_f\left(\mathcal{A}^T\nabla w\right)^T\cdot[\![u]\!]+[\![w]\!]^T\cdot(\mathcal{A}\nabla u)+[\![w]\!]\cdot\left(\mathcal{A}\eta_f r_f([\![u]\!])\right)\,d\Gamma\\ &-\sum_{f\in\Gamma_B}\int_f\left(\mathcal{A}_B^T\nabla w^+\right)^T\cdot\left(u^+-u_B\right)-\left(w^+n^+\right)^T\cdot\mathcal{A}_B\nabla u^B\,d\Gamma\\ &-\sum_{f\in\Gamma_B}\int_f\left(w^+n^+\right)^T\cdot\mathcal{A}_B\eta_f r_f\left(\left(u^+-u_B\right)n^+\right)\,d\Gamma, \quad (1.9)\end{aligned}$$

where $\mathcal{A}_B$ is the viscous diffusion tensor evaluated at the boundary, r is the lifting operator, and η_e is the BR2 stabilization parameter which must be greater than or equal to the number of faces in an element. The lifting operator is defined on an interior face (f) by,

$$0=\sum_{k\in k_f}\int_k\tau^T\cdot r_f(q)\,d\Omega+\int_f\{\tau\}^T\cdot q\,d\Gamma\quad\forall\tau,q\in[\mathcal{W}_{h,p}]^d, \quad (1.10)$$

and on the boundary by,

$$0=\int_{k_B}\tau^T\cdot r_f(q)\,d\Omega+\int_f\tau^{+T}\cdot q\,d\Gamma\quad\forall\tau,q\in[\mathcal{W}_{h,p}]^d. \quad (1.11)$$

The set of elements sharing the interior face (f) is k_f, and the element on the interior of a boundary face is k_B. Essentially, the lifting operator penalizes the gradient on u based on the jumps present between elements.

The DG discretization of a source term ($S(u)$) is given by,

$$R_{h,p}^{source}(u,w)=\sum_{k\in\mathcal{T}_h}\int_{\Omega_k}w^TS(u)\,d\Omega. \quad (1.12)$$

In the DG method, the solution is represented as a polynomial defined piecewise within each element. This means straight-sided elements are not required by the

DG method. Instead, we can use elements with curved faces. This is advantageous since approximating a curved geometery with straight-sided elements introduces a discretization error that scales with the characteristic size of the mesh.

Since the integrals present in the DG method cannot be performed analytically, we use Gaussian Quadrature to approximate the integrals. The order of the quadrature is dependent on the order of the approximtation space (p) as $3\left(p+2\right)-1$. Note that it is independent of whether the grid is curved or straight sized.

1.2.1. Shock Capturing. To regularize the solution around shocks, an artificial viscosity term added to the Navier-Stokes equations. The artificial viscosity formulation is based on the work of Barter and Darmofal [1], and Yano [8]. An additional PDE is solved to drive the artificial viscosity, which we will refer to as the 'sensor PDE'. The sensor PDE used to create a smooth shock-sensor field (s) is given by,

$$0 = \nabla \cdot \left(\eta \nabla s\right) + \left[C_3 \tilde{S}_k\left(u\right) - s\right], \tag{1.13}$$

where $\eta_{ij} = C_2 \mathcal{H}_{ik} \mathcal{H}_{kj}$. This PDE is sovled subject to Robin boundary conditions,

$$\eta_{ij} \frac{\partial s}{\partial x_j} n_i + \sqrt{C_2} n_i \mathcal{H}_{ij} n_j s = 0. \tag{1.14}$$

with coefficients,

$$C_2 = 5 \quad C_3 = 1. \tag{1.15}$$

We use Barter's element-based source term [1] to drive the sensor PDE,

$$J_k\left(u\right) = \frac{1}{\left|\partial\kappa\right|} \int_{\partial\kappa} \left| \frac{\left[\!\left[g\left(u\right)\right]\!\right]}{\left\{g\left(u\right)\right\}} \right| d\Gamma, \tag{1.16a}$$

$$\xi\left(J_k\right) = \log_{10}\left(J_k + 10^{-16}\right), \tag{1.16b}$$

$$\xi_0 = 3 + 2\log_{10} P + 0.5, \tag{1.16c}$$

$$\tilde{S}_k\left(u\right) = f_{switch}\left(\frac{\xi\left(J_k\left(u\right)\right) - \xi_0}{\Delta\xi}; 10\right), \tag{1.16d}$$

where P is the polynomial order of the basis functions used. This sensor is driven by inter-element jumps in a solution quanity ($g\left(u\right)$), which we are free to specify. In this paper we have used inter-element pressure jumps to detect shocks (i. e. $g\left(u\right) = p$). The parameter $\Delta\xi$ governs the width over which the switch goes from fully on to fully off. We use $\Delta\xi = 2$, which means the switch turns on over 2 orders of magnitude change in J_k. The non-linear switch is given by,

$$f_{switch}\left(\xi;\alpha\right) = \xi + \frac{1}{\alpha}\log\left[1 - \frac{e^{-\alpha(1-\xi)} - e^{-\alpha\xi}}{e^{-\alpha(1-\xi)} - 1}\right]. \tag{1.17}$$

We interpret the sensor variable (s) as the inverse of the Peclet number required locally. So the artificial viscosity is calculated from the solution to the sensor PDE as,

$$\epsilon_{ij} = \frac{2}{p}\lambda\left(u\right)\mathcal{H}_{ij}\max\left\{0, s\right\}. \tag{1.18}$$

A final correction is applied such that this artificial viscous term is applied to $\nabla(\rho H)$, rather than $\nabla(\rho E)$. Thats is the flux due to the artificial viscosity is given by,

$$\mathbf{F}_{AV} = \epsilon \nabla \begin{bmatrix} \rho \\ \rho \mathbf{V} \\ \rho H \end{bmatrix}. \tag{1.19}$$

This is the final viscous term added to the Navier-Stokes equations to regularize the solution around shocks.

1.2.2. Error Estimation. We now give an overview of the error estimation methodology used. A more complete discussion can be found ny Yano[8]. Consider an output function derived from the solution to the PDE, J (in this case the heat flux over the surface). The error between the approximation (based on the discrete PDE solution) and the true value can be defined as,

$$\mathcal{E}_{true} = J(u) - J(u_{h,p}). \tag{1.20}$$

Using dual weighted residual (DWR) methodology described by Becker and Rannacher[3], this error can be written as,

$$\mathcal{E}_{true} = -R_{h,p}(u_{h,p}, \psi), \tag{1.21}$$

where ψ is the adjoint solution given by,

$$\bar{R}'_{h,\hat{p}}[u, u_{h,p}](w, \psi) = \bar{J}'_{h,\hat{p}}[u, u_{h,p}](w) \quad \forall w \in \mathcal{W}. \tag{1.22}$$

The quantities $\bar{R}'_{h,\hat{p}}$ and $\bar{J}'_{h,\hat{p}}$ are mean-value linearizations,

$$\bar{R}'_{h,\hat{p}}[u, u_{h,p}](w, v) = \int_0^1 R'_{h,\hat{p}}[(1-\theta)u + \theta u_{h,p}](w, v)\, d\theta, \tag{1.23}$$

$$\bar{J}'_{h,\hat{p}}[u, u_{h,p}](w) = \int_0^1 J'_{h,\hat{p}}[(1-\theta)u + \theta u_{h,p}](w)\, d\theta. \tag{1.24}$$

The Frechet derivatives of R and J about u with respect to w (i. e. the first argument) are denoted by $R'_{h,\hat{p}}[u]$ and $J'_{h,\hat{p}}[u]$ respectively.

Since the true adjoint solution is not available, an approximation to the adjoint in an enriched space (we use $\hat{p} = p + 1$) linearized about $u_{h,p}$ is obtained by solving the problem,

$$R'_{h,\hat{p}}[u_{h,p}](w_{h,\hat{p}}, \psi_{h,\hat{p}}) = J'_{h,\hat{p}}[u_{h,p}](w_{h,\hat{p}}) \quad \forall w_{h,\hat{p}} \in \mathcal{W}_{h,\hat{p}}. \tag{1.25}$$

We can now obtain the DWR error estimatate approximation,

$$\mathcal{E} \approx -R_{h,p}(u_{h,p}, \psi_{h,\hat{p}}). \tag{1.26}$$

Finally, the local error estimate (η_k) corresponding to element k is defined as,

$$\eta_k = |R_{h,p}(u_{h,p}, \psi_{h,\hat{p}}|_k)|. \tag{1.27}$$

1.3. Blottner Sphere. We have chosen to use the sphere case examined by Blottner[4] for our investigation. Blottner used a shock-fitting axisymmetric Navier-Stokes code to obtain high quality heat flux results, which we use as our reference values.

The Blottner sphere is in a Mach 5 flow, with a Reyonlds Number (based on sphere diameter) of 1.8875×10^6. Using a diameter of $0.127m$, we obtain the following inflow conditions in Table 1.1. The wall temperature is $98.89K$.

2. Two-Dimensional Results. We start by examining a two dimensional analogue before performing full $3D$ calculations. Heat flux results are obtained for a $2D$ cylinder with the same diameter as Blottner's Sphere. Since Blottner only provides results for a sphere, we correct the stagnation heatflux from axisymmetric to $2D$ according to Equation 1 of Reference [6]. We use this as our reference value, however it is important to note that this is an *approximation* to the stagnation point heat flux, so it is considered a guide rather than the truth value.

2.1. Provided $Q1$ Grids. We start by calculating the heat flux over the sphere using a family of $Q1$ grids which are considered best practice for finite volume calculations. The grid parameters are given in Table 2.1. These are structured quadrilateral grids with the same number of elements in each direction.

In Figure 2.1b the near-wall region of Grid 2 is shown, where we have reflected the grid in $x = 0$, and overlayed the upper and lower portions of the grid. Note that the upper and lower portions of the grid do not lay over each other – that is the grid is slightly asymmetric. This manifests in an asymmetry in the heat flux of order 1% on the coarsest grid.

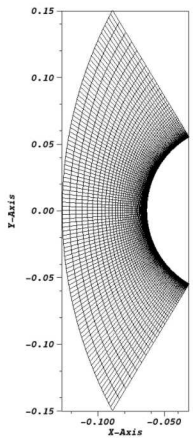

(a) Grid 2

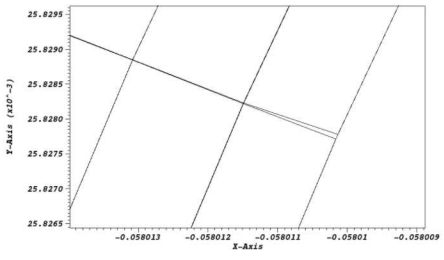

(b) Comparison of upper and lower near-wall grids

Fig. 2.1: Grid 2

The DG het flux results on this family of grids are given in Figure 2.2, along with the finite volume results on the same grid. As the grid resolution is increased, the quality of the predictions improve. Moving away from the stagnation point, the DG results tend to overpredict the heat flux. This overheating reduces as the grid is

refined. This is due to the fact that the sensor variable is non-zero in the boundary layer away from the stagnation point.

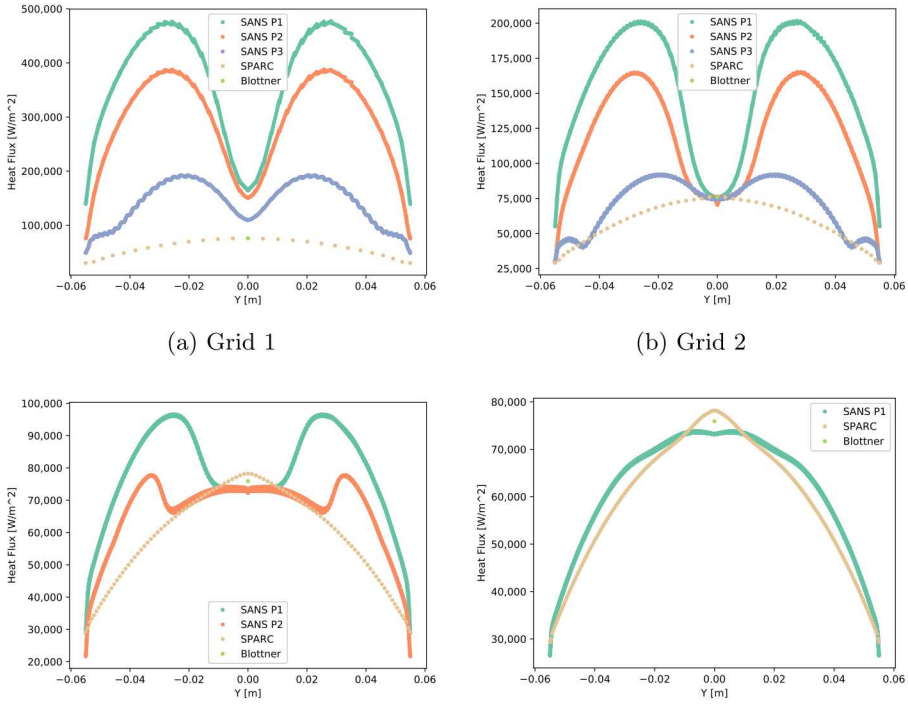

(a) Grid 1

(b) Grid 2

(c) Grid 3

(d) Grid 4

Fig. 2.2: Heat flux predicted using provided $Q1$ quadrilateral grids

The adjoint $P1$ solutions are given in Figures 2.3 to 2.18 for Grids 1 to 4 repectively. All of the adjoints exhibit oscillation in the boundary layer. While the extent of these oscillations reduces as the number of elements increases, the oscillations are present even in the finest grid.

The error indicator predicted by the DWR is given in Figures 2.19 to 2.22 for $Q1$ Grids 1 to 4 respectively. As both the order is increased and the grid is refined, the sources of error in the integrated heat flux narrow to the shock, the boundary layer, and the stagnation streamline. Increasing the grid resolution shifts the source of error from being approximately equal between the shock and the boundary layer, to the shock being the most significant contribution to the error. As the order of the solution increases, the ratio of the shock and boundary layer resolutions remains approximately fixed. Note that on these $Q1$ grids, the inability of the grid to account for the curvature of the sphere introduces error near the boundary in the higher-order results.

2.2. Provided $Q3$ Grids. Since the quality of solution using higher-order DG is known to be poor when using $Q1$ grids, the provided $Q1$ grids are projected to $Q3$, by interpolation in the (r, θ)-space to generate the higher-order nodes. These grids share the same slight near-wall asymmetry of the original $Q1$ grids.

The poor quality heat fluxes in Figure 2.24a is due to the fact that the grid around the boundary layer is relatively coarse. This results in a non-zero sensor value in the boundary layer for the $P2$ and $P3$ results, as can be seen in Figure 2.25. Thus there is non-zero artificial viscosity in the boundary layer, which is the cause of the poor quality heat fluxes.

The surface pressure profiles are given in Figure 2.26, and the surface shear profiles are given in Figure 2.27. There is good agreement between the finite volume and DG results, except on Grid 1, where the effect of the artificial viscosity in the boundary layer can be seen in both the pressure and shear stress profiles.

The primal $P1$ solutions are given in Figures 2.28 to 2.31 for Grids 1 to 4 repectively. Note that while the maximum sensor value remains approximately constant as the grid resolution is varied, the artificial viscosity applied is proportional to the grid size (see Equation 1.18), so the artificial viscosity decreases as the grid resolution increases.

The density, velocity and temperature profiles along the stagnation line are given in Figure 2.32 to 2.43, with the results from SPARC for comparison. While the density and temperature results are similar, we can see that velocity profiles in the boundary layer are converging to different profiles.

The adjoint $P1$ solutions are given in Figures 2.44 to 2.59 for Grids 1 to 4 repectively. Since Grid 1 is so coarse, the adjoint result for that grid is of low quality, and exhibits instability in the boundary layer (e. g. see Figure 2.44a). On the finer grids, the adjoint features are primarily the bounday layer, and the stagnation streamline. The sensor equation adjoint is active almost exclusively in the boundary layer, however on the finest grids, a feature can be seen where the shock intersects the stagnition streamline.

The $P3$ adjoints on the coarsest grid are given in Figures 2.60 and 2.61. This corresponds to one of the low quality heat flux results in 2.2a. We can see significantly more oscillation in these results than the $P1$ results, which indicates that the grid resolution is insufficient to capture the adjoint solution correctly. This feature is at the sonic line, and is due to the log-type signularity that occurs in the Euler equations when flow accelerated from subsonic to supersonic Mach numbers[5].

The DG results on these grids are given in Figure 2.24, along with the finite volume results on the same grid. As the grid resolution is increased, the quality of the predictions improve. Comparing to the $Q1$ results, we can see that a significant improvement in the quality of the DG results is obtained due to curving the grid to better conform to the spherical surface. In fact, the results are now comparable in quality to the finite volume results on the same grid.

The improvement in the result moving from a $Q1$ to a $Q3$ grid is so striking due to the artificial viscosity method used. The artificial viscosity is driven by a resolution detector. That is the source term in the sensor PDE is designed to be active in regions where the resolution of the grid is insufficient to resolve the solution features. This is the case in the boundary layer for the $Q1$ grids, due to a curved geometry being approximated with straight sides. This results in a non-zero sensor field in the boundary layer (leading to non-zero artificial viscosity) for the $Q1$ case, which is not present in the $Q3$ case (see Figure 2.62).

The error indicator predicted by the DWR is given in Figures 2.63 to 2.66 for $Q3$ Grids 1 to 4 respectively. While the trends are similar to those for the error indicator on the $Q1$ grids, the magnitude of the error contribution due to the boundary layer mesh resolution is significantly reduced. The grid resolution at the shock around the

stagnation streamline is now the prime contributor to the error.

Our results exhibit two limiting cases of boundary layer resolution. The first is when the boundary layer is too coarse, which results in poor heat flux predictions (see Figure 2.24a). In this case we can see oscillations in the adjoint (Figures 2.44, and 2.60), as well as significantly higher error indicator values (Figure 2.63). The second limit is when the boundary layer is sufficiently refined that the artificial viscosity is essentially zero in the boundary layer. In this case, the heat flux is converging, the adjoints as well behaved, and the error indiciator shows that the error in the heatflux is primarily driven by the shock.

2.3. Synthesis. The variation of stagnation and surface integrated heat fluxes with degrees of freedom are given in Figures 2.68 and 2.69 respectively. We use the Gaussian weighted surface heat flux centered on the stagnation point as the stagnation heat flux for the DG results. Projecting from the $Q1$ grids to $Q3$ results in a significant improvement to the quality of the DG results. Using high-order grids, it is possible to obtain DG heat flux results that are comparable to finite volume results.

3. Three-Dimensional Results. The heat flux over a $120K$ element grid of $Q1$ hexerhedrals is shown in Figure 3.1. The heat flux matches the stagnation point value from Blottner and the finite volume result well. However, it exhibits the same overheating away from the stagnation point that the $Q1$ cylinder results have. Based on the difference between the $Q1$ and $Q3$ cylinder results, we expect this is a feature of using a $Q1$ grid. The DG heat flux also exhibits has the same 'grid imprinting' phenomenon as the SUPG results in Figure 3.2.

We suspect the 'grid imprinting' in the DG results is due to the grid at the wall, particularly when using a $Q1$ grid. The sensor equation (which drives the artificial viscosity) is essentially a resolution indicator. Near the surface of the sphere, the $Q1$ grid poorly approximates the true geometry of the sphere, which causes generation of the sensor variable. Since the sensor is non-zero in the boundary layer, artificial viscosity is applied in the boundary layer which is a function of the grid size (see Equation 1.18). Thus, in the region where the size of the surface grid rapidly increses, the artificial viscosity also increases rapidly, which is shown in Figure 3.3.

In Figure 3.4 the error indicator is shown for horizontal and 45^o inclined slices through the domain normal to the sphere. Both the shock and the boundary layer regions are significant sources of error in the domain. The sudden increase in error in the boundary layer region corresponds to where the surface grid size also abruptly changes.

The error indicator over the surface of the sphere is given in Figure 3.5. We can see that a significant contribution to the error in the integrated heat flux comes from the elements on the surface of the sphere. Furthermore, the error contribution increases by nearly two-orders of magnitude in the region corresponding to 'grid imprinting'. This, combined with the artificial viscosity result in Figure 3.3, suggests that it is the sudden change in the size of elements on the surface of the sphere that results in the 'grid imprinting' observed in heat flux.

4. Conclusions. The prediction of heat flux over a sphere in hypersonic flow is an interesting and challenging problem. When using solutions to the Navier-Stokes equations to predict the heat flux, a common source of numerical error is a phenomenon known as 'grid imprinting'. Rather than the axisymmetric heat flux profile expected for a spherical surface, the topology of the grid can be seen in the surface heat flux distribution. We have examined the origin of this phenomenon; specifically

the regions of the grid that contribute most. Comparisons have been made between second order finite volume and Discontinuous Galerkin results, where the DG results ranged from 2^{nd} to 4^{th} order. The Dual Weighted Residual framework was used to obtain local error estimates for the heat flux integrated over the surface with respect to the grid for the DG results.

We now refer back to our original research questions.

Can we get good quality high-order heat fluxes on cylinders and spheres?

Based on the results from the cylinders in two-dimensions, a curved (higher-order) grid is important for obtaining good quality heat fluxes in the case. This can be seen in the primal solution, where the sensor is non-zero (and significant) in the boundary layer for the $Q1$ grids. The non-zero sensor field results in artificial viscosity being applied in the boundary layer, which degrades the quality of the heat fluxes significantly. The error indicator also shows that in the $Q1$ cases, the resolution of the grid near the wall contributes much more to the error in heat flux than in the $Q3$ case.

Can we use features of the numerical solution to understand the error sources?

The adjoint and error indicator results show that our $Q3$ results span two limiting cases of grid resolution. The coarsest grid is too coarse in the boundary layer, which leads to poor heat flux predictions. The coarseness of the grid can be seen reflected in the adjoints, where there is significant oscillation, as well as significantyl higher values of the error indicator. The second limit is when the boundary layer is sufficiently refined that the artificial viscosity is essentially zero in the boundary layer and the hat flux is converging. In this case the adjoints do not exhibit and oscillations, and the error indicator shows that the error is primarily driven by the grid resolution at the shock.

What is the origin of this grid imprinting?

The 'grid imprinting' appears to be driven by the sudden change in the size of surface elements. At the resolution that the sphere case was run at, the sensor is non-zero in the boundary layer. Since the artificial viscosity is proportional to the grid spacing, as the size of elements on the surface rapidly increases, so does the artificial viscosity.This is reflected in the error indicator, which increases by nearly two-orders of magnitude as the surface elements rapidly increase in size. That is, the error indicator shows that the error in integrated heat flux has significant contributions from the large elements on the surface of the sphere.

5. Future Work. As a result of this investigation, we have two new research questions:

- **Does using curved grids in 3D alleviate grid imprinting?** Based on the results for the cylinders, we would expect curved grids to significantly reduce the magnitude of the sensor variable, and so artificial viscosity, in the boundary layer. Since the artificial viscosity is element-size dependent, it is reasonable to expect curved grids to reduce the 'grid imprinting'. However, based on this work it is not clear if there are other contributing factors to the 'grid imprinting' which are unaffected by the grid curvature. To be able to reliably predict high quality heat fluxes on these geometries, it is necessary to further investigate the extent that curved grids improves heat fluxes in 3D configurations
- **Does output based mesh adaptation alleviate grid imprinting?** If 'grid imprinting' is primarily caused by the rapid change in surface grid size,

as the error indicator results suggest, then adapting the grid to reduce the error in integrated heat flux (e. g. using the MOESS framework[8]) should reduce 'grid imprinting', and result in a grid whose surface elements vary smoothly in size. If output based mesh adapation is able to produce high quality heat fluxes for reasonable computational expense, it would reduce the effort required in grid generation for the user, and the dependence of the quality of the final result on the grid generated.

Acknowledgement. Sandia National Laboratories is a multimission laboratory managed and operated by National Technology & Engineering Solutions of Sandia, LLC, a wholly owned subsidiary of Honeywell International Inc., for the U.S. Department of Energys National Nuclear Security Administration under contract DE-NA0003525.

REFERENCES

[1] G. E. Barter and D. L. Darmofal, *Shock capturing with PDE-based artificial viscosity for DGFEM: Part I. formulation*, J. Comput. Phys., 229 (2010), pp. 1810–1827.

[2] F. Bassi and S. Rebay, *GMRES Discontinuous Galerkin solution of the compressible Navier-Stokes equations*, in Discontinuous Galerkin Methods, B. Cockburn, G. E. Karniadakis, and C.-W. Shu, eds., Berlin, Heidelberg, 2000, Springer Berlin Heidelberg, pp. 197–208.

[3] R. Becker and R. Rannacher, *An optimal control approach to a posteriori error estimation in finite element methods*, Acta Numerica, 10 (2001), p. 1102.

[4] F. G. Blotter, *Accurate Navier-Stokes results for the hypersonic flow over a spherical nosetip*, Journal of Spacecraft and Rockets, 27 (1990), pp. 113–122.

[5] M. B. Giles and N. A. Pierce, *Analytic adjoint solutions for the quasi-one-dimensional euler equations*, Journal of Fluid Mechanics, 426 (2001), pp. 327–345.

[6] H. H. Hamilton II, *Approximate method of calculating heating rates at general three-dimensional stagnation points during atmospheric entry*, Tech. Rep. NASA-TM-84580, NASA Langley Research Center; Hampton, VA, United States, November 1982.

[7] B. S. Kirk, S. W. Bova, and R. B. Bond, *The influence of stabilization paraneters in the SUPG finite elment method for hypersonic flows*, in 48th AIAA Aerospace Sciences Meeting Including the New Horizons Forum and Aerospace Exposition, American Institute of Aeronautics and Astronautics, 2010.

[8] M. Yano, *An optimization framework for adaptive higher-order discretizations of partial differential equations on anisotropic simplex meshes*, PhD thesis, Massachusetts Institute of Technology. Dept. of Aeronautics and Astronautics, 2012.

Property	Value
Density $[kg/m^3]$	8.788×10^{-2}
Velocity $[m/s]$	871.47
Temperature $[K]$	75.58

Table 1.1: Inflow conditions

Index	Elements	Wall Normal Spacing [m]
1	$2,500$	1.6×10^{-6}
2	$10,000$	8×10^{-7}
3	$40,000$	4×10^{-7}
4	$160,000$	2×10^{-7}

Table 2.1: $Q1$ quad. grid parameters

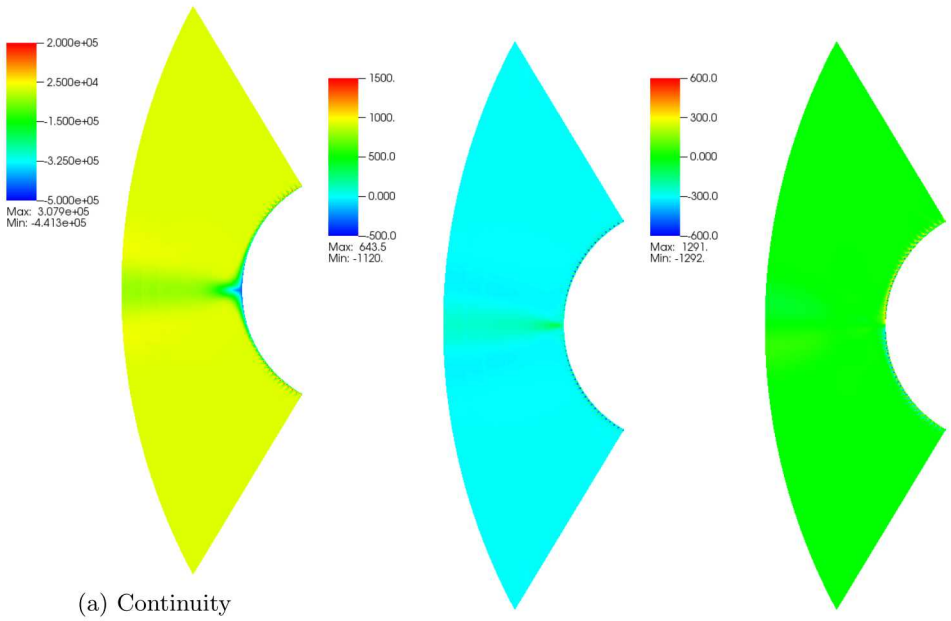

(a) Continuity

(b) X-momentum

(c) Y-momentum

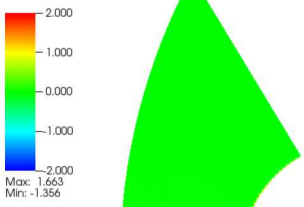

(d) Total internal energy

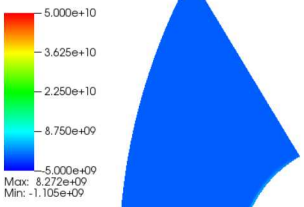

(e) Sensor

Fig. 2.3: Adjoint P1 solution on $Q1$ Grid 1

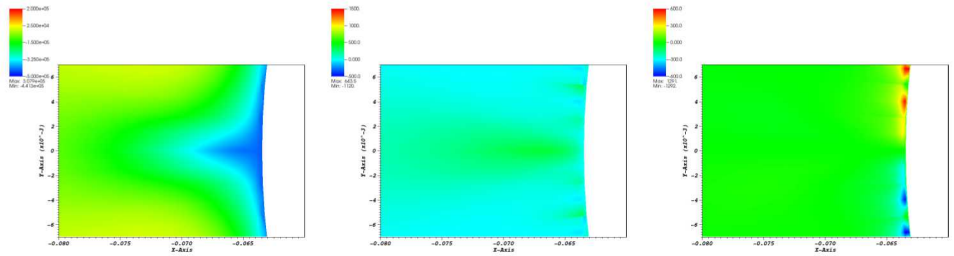

(a) Continuity (b) X-momentum (c) Y-momentum

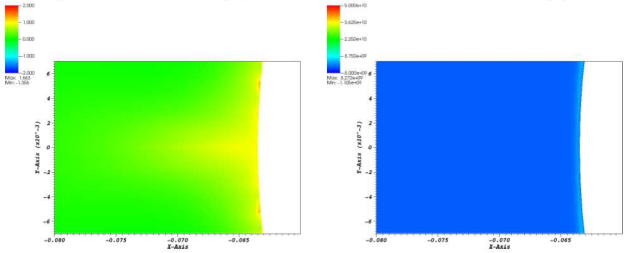

(d) Total internal energy (e) Sensor

Fig. 2.4: Adjoint P1 solution on $Q1$ Grid 1, focus on stagnation point

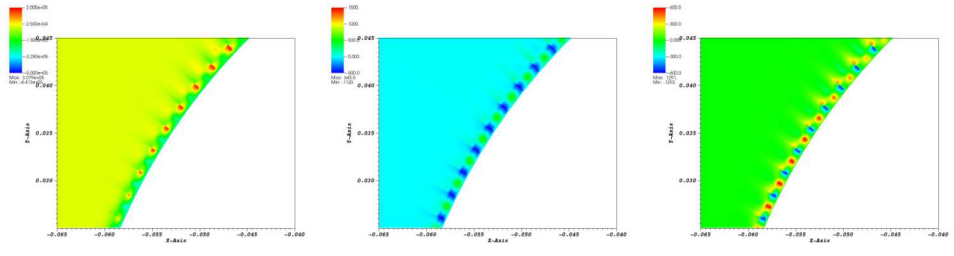

(a) Continuity (b) X-momentum (c) Y-momentum

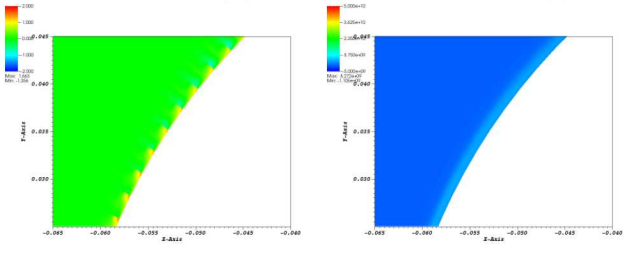

(d) Total internal energy (e) Sensor

Fig. 2.5: Adjoint P1 solution on $Q1$ Grid 1, focus on surface half way around computational domain

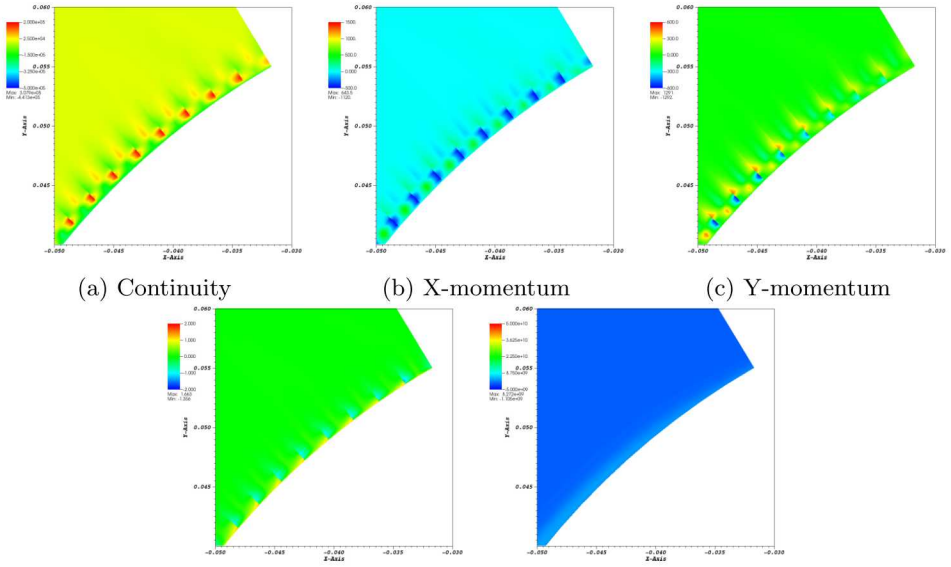

(a) Continuity (b) X-momentum (c) Y-momentum

(d) Total internal energy (e) Sensor

Fig. 2.6: Adjoint P1 solution on $Q1$ Grid 1, focus on surface at edge of computational domain

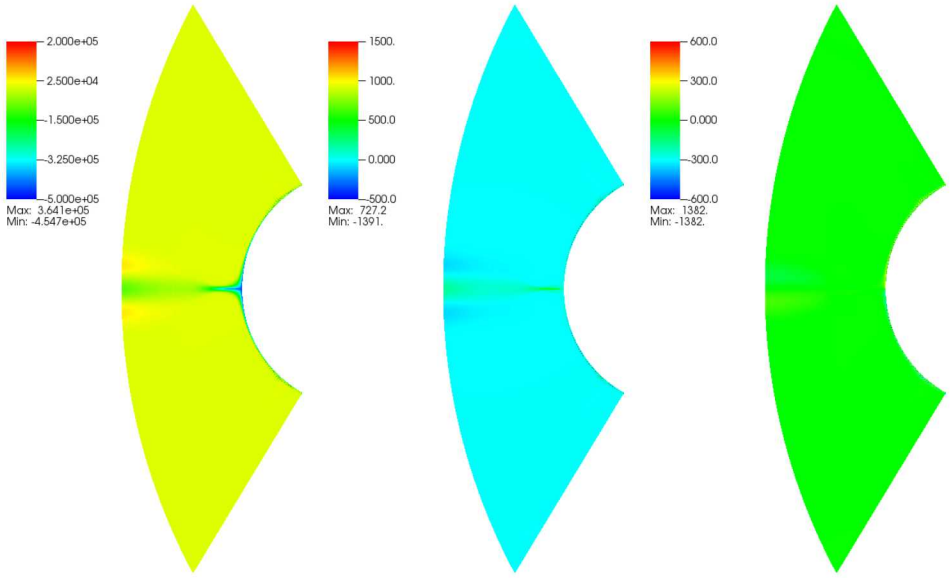

(a) Continuity (b) X-momentum (c) Y-momentum

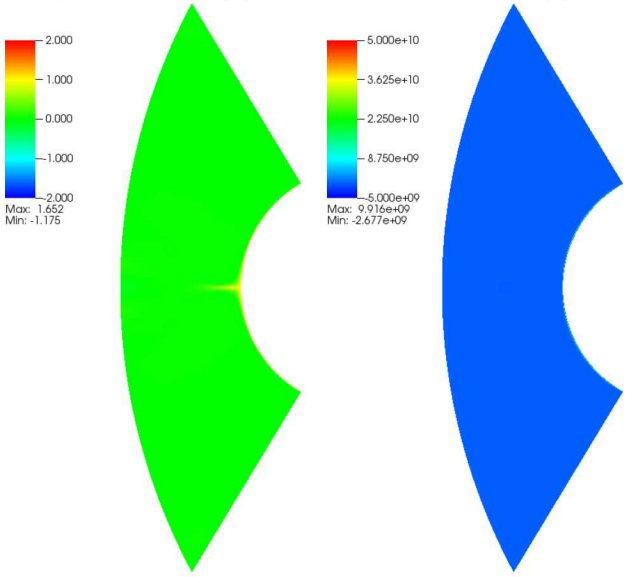

(d) Total internal energy (e) Sensor

Fig. 2.7: Adjoint P1 solution on $Q1$ Grid 2

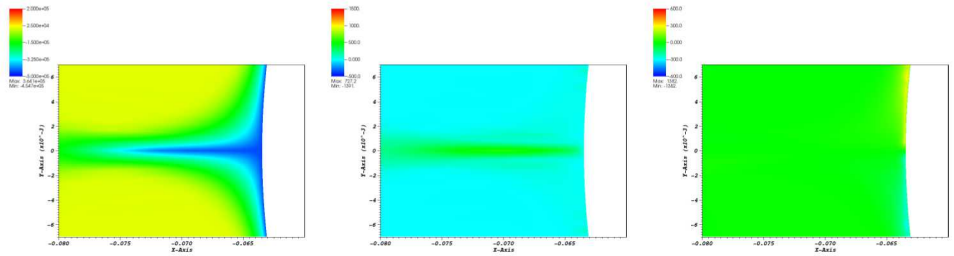

(a) Continuity (b) X-momentum (c) Y-momentum

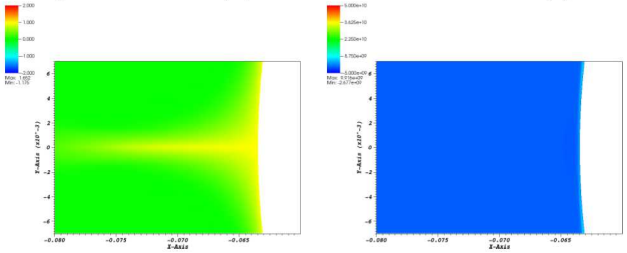

(d) Total internal energy (e) Sensor

Fig. 2.8: Adjoint P1 solution on $Q1$ Grid 2, focus on stagnation point

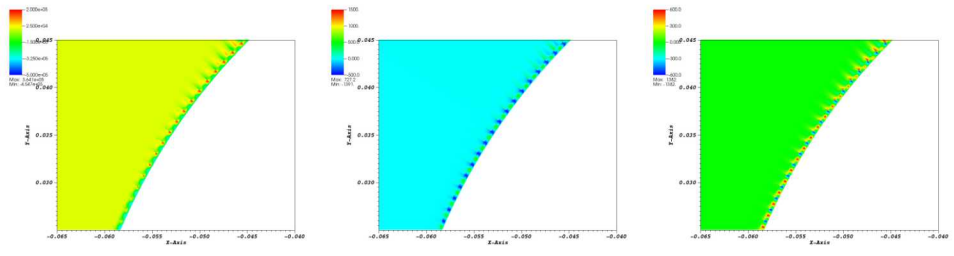

(a) Continuity (b) X-momentum (c) Y-momentum

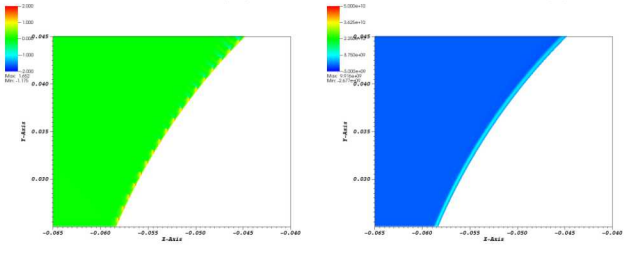

(d) Total internal energy (e) Sensor

Fig. 2.9: Adjoint P1 solution on $Q1$ Grid 2, focus on surface half way around computational domain

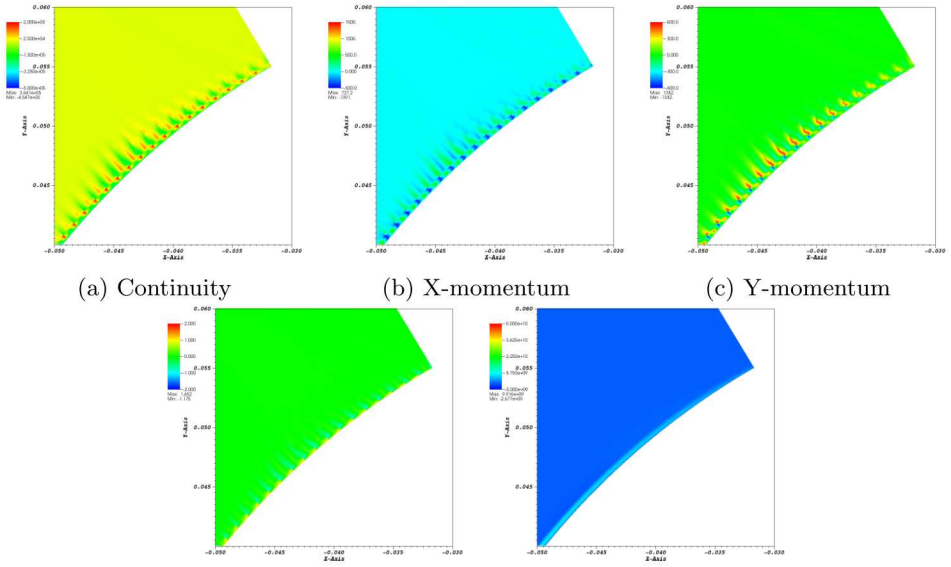

(a) Continuity (b) X-momentum (c) Y-momentum

(d) Total internal energy (e) Sensor

Fig. 2.10: Adjoint P1 solution on $Q1$ Grid 2, focus on surface at edge of computational domain

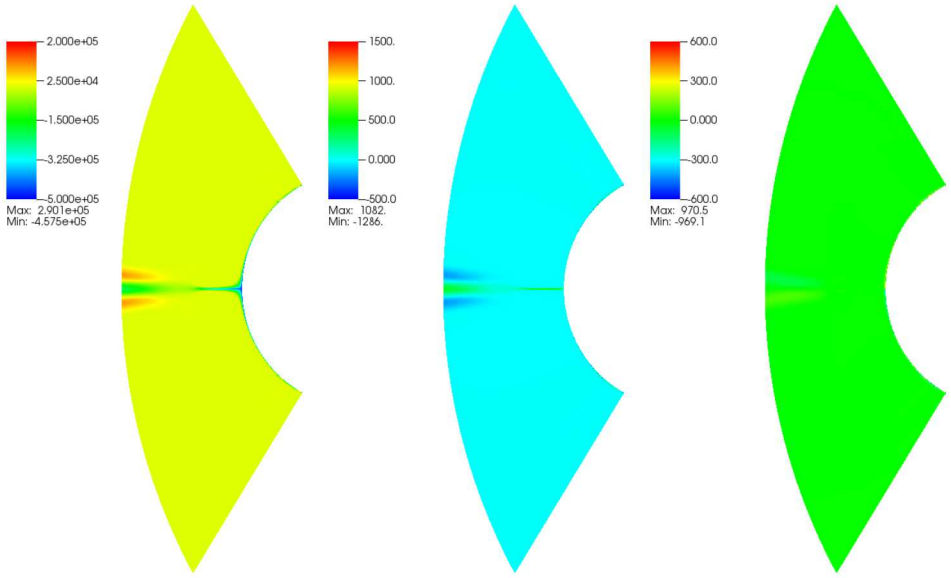

(a) Continuity (b) X-momentum (c) Y-momentum

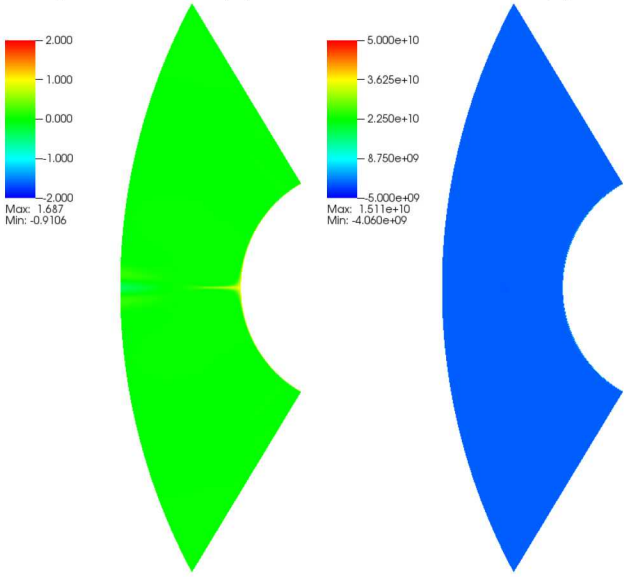

(d) Total internal energy (e) Sensor

Fig. 2.11: Adjoint P1 solution on $Q1$ Grid 3

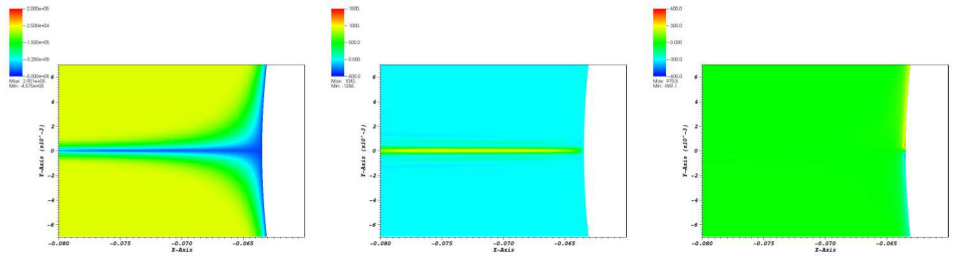

(a) Continuity (b) X-momentum (c) Y-momentum

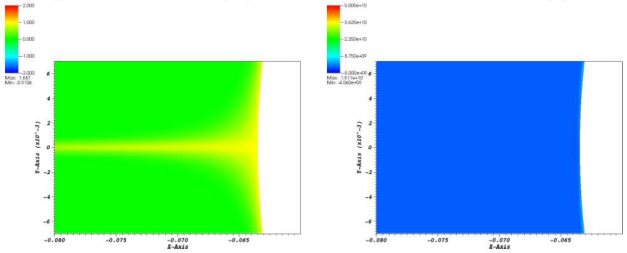

(d) Total internal energy (e) Sensor

Fig. 2.12: Adjoint P1 solution on $Q1$ Grid 3, focus on stagnation point

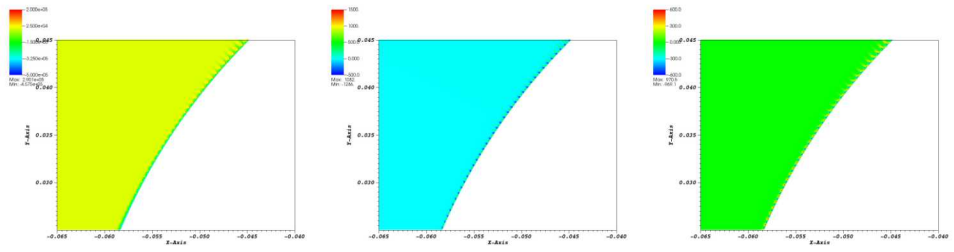

(a) Continuity (b) X-momentum (c) Y-momentum

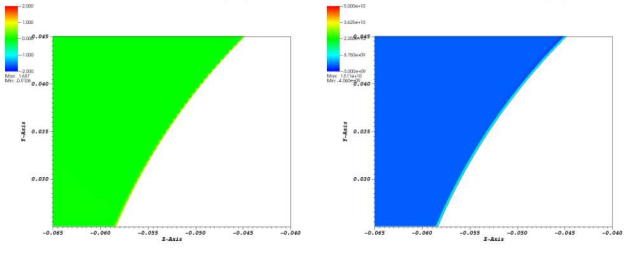

(d) Total internal energy (e) Sensor

Fig. 2.13: Adjoint P1 solution on $Q1$ Grid 3, focus on surface half way around computational domain

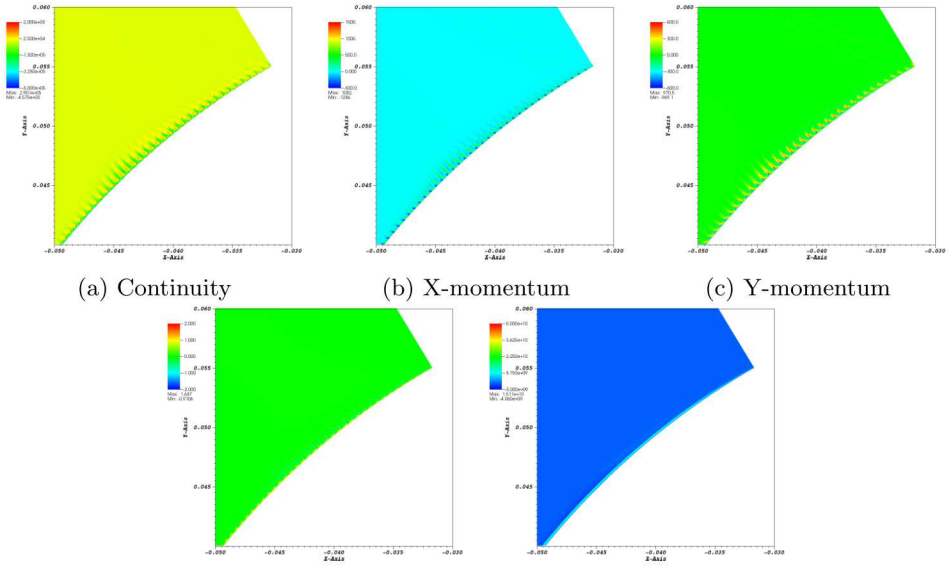

(a) Continuity (b) X-momentum (c) Y-momentum

(d) Total internal energy (e) Sensor

Fig. 2.14: Adjoint P1 solution on $Q1$ Grid 3, focus on surface at edge of computational domain

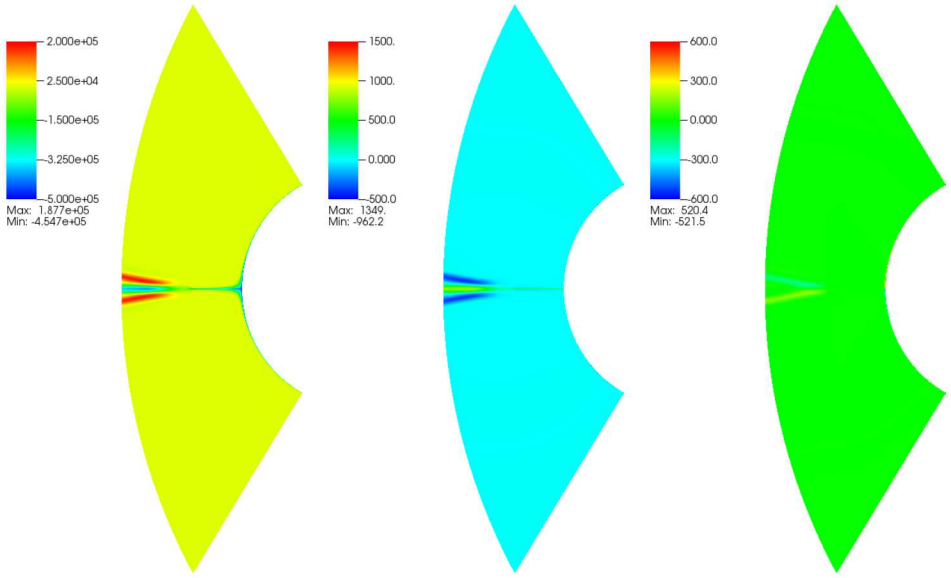

(a) Continuity (b) X-momentum (c) Y-momentum

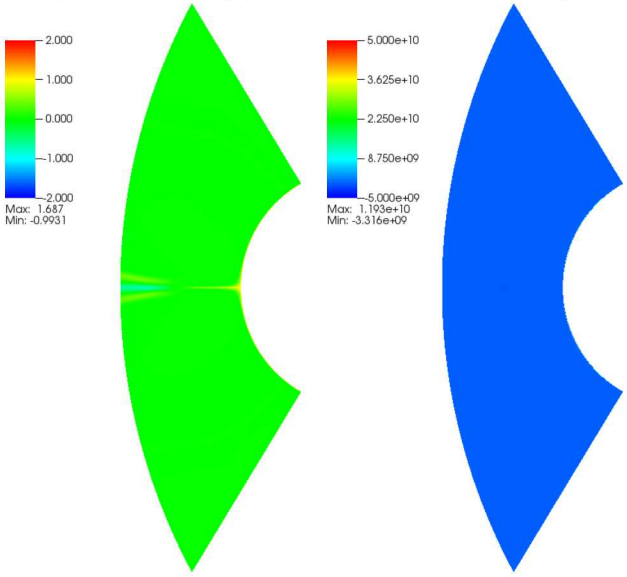

(d) Total internal energy (e) Sensor

Fig. 2.15: Adjoint P1 solution on $Q1$ Grid 4

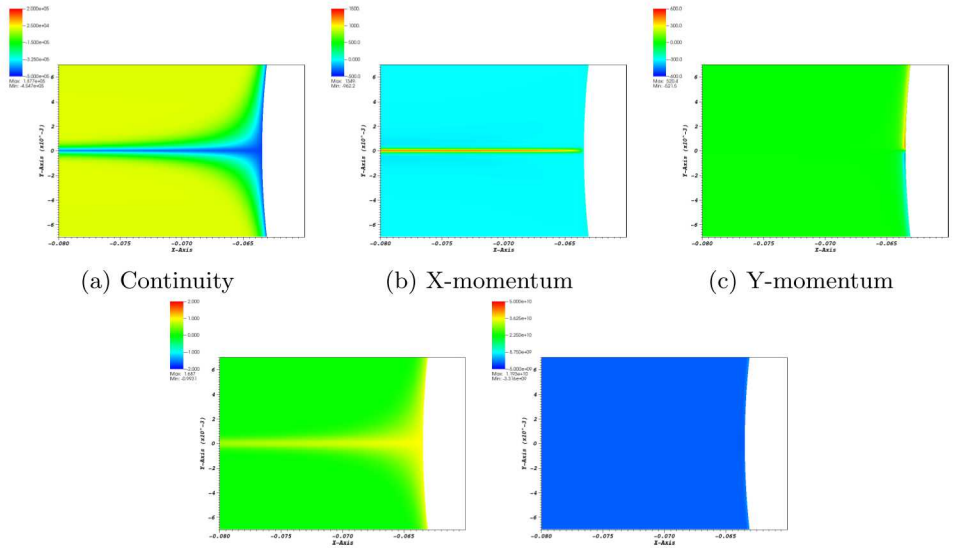

(a) Continuity (b) X-momentum (c) Y-momentum

(d) Total internal energy (e) Sensor

Fig. 2.16: Adjoint P1 solution on $Q1$ Grid 4, focus on stagnation point

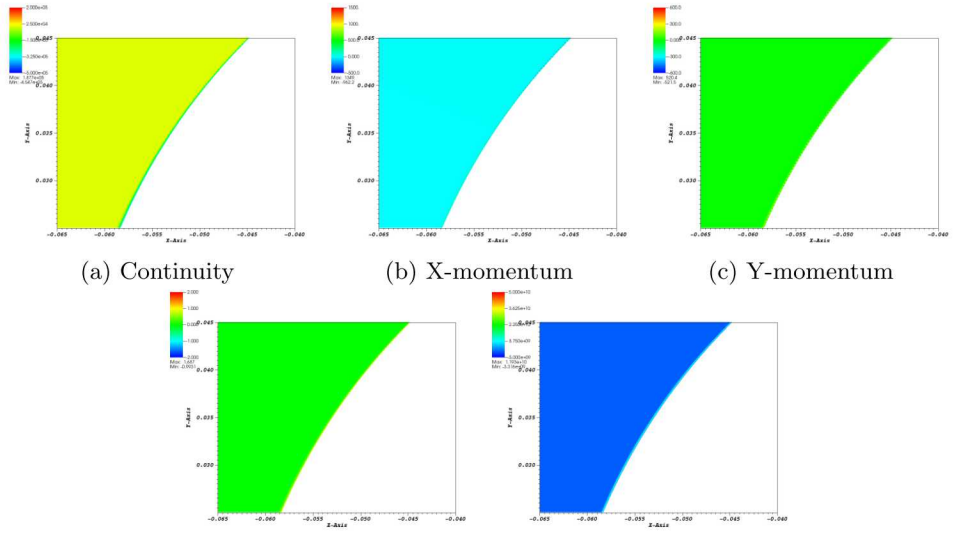

(a) Continuity (b) X-momentum (c) Y-momentum

(d) Total internal energy (e) Sensor

Fig. 2.17: Adjoint P1 solution on $Q1$ Grid 4, focus on surface half way around computational domain

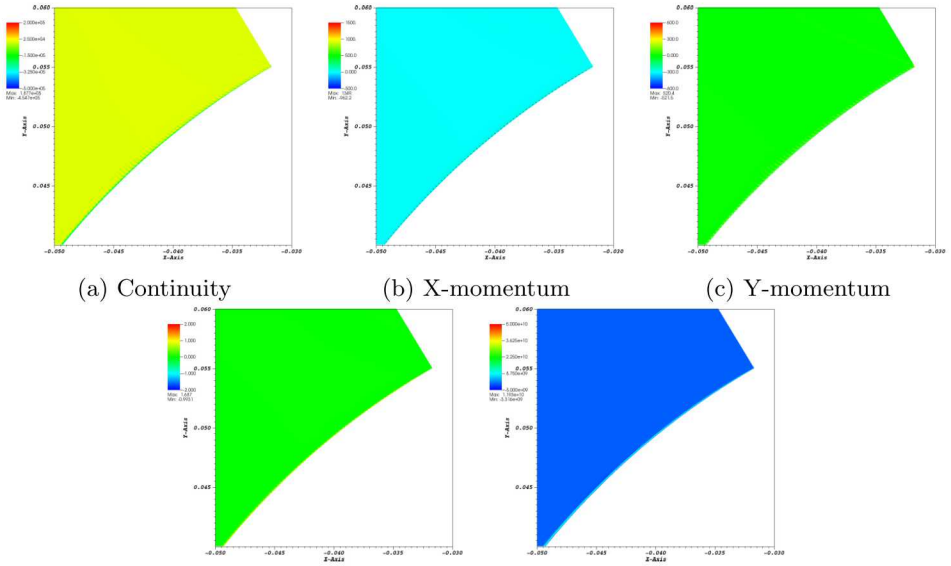

(a) Continuity (b) X-momentum (c) Y-momentum

(d) Total internal energy (e) Sensor

Fig. 2.18: Adjoint P1 solution on $Q1$ Grid 4, focus on surface at edge of computational domain

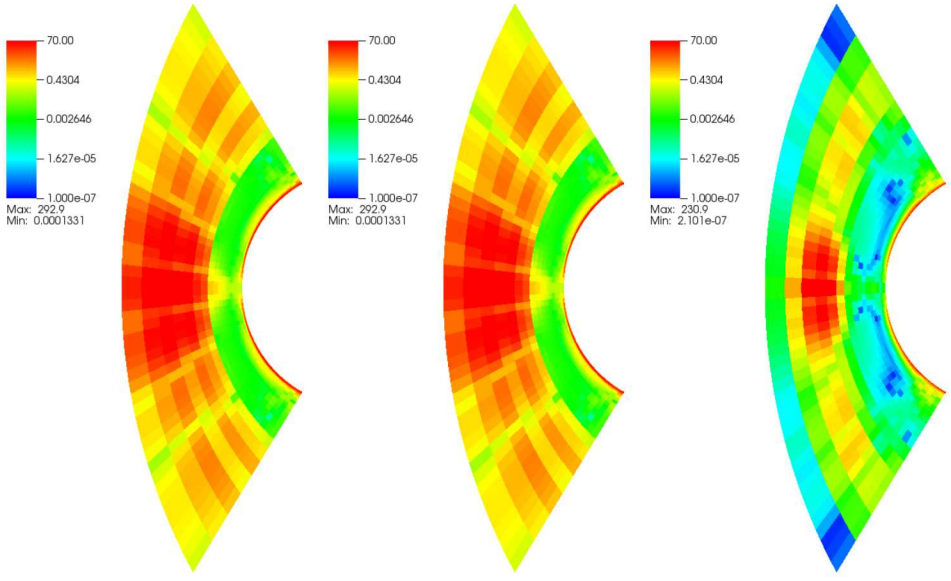

(a) P1 (b) P2 (c) P3

Fig. 2.19: Error indicator on Grid 1 for integrated surface heat flux using $Q1$ quadrilateral grids

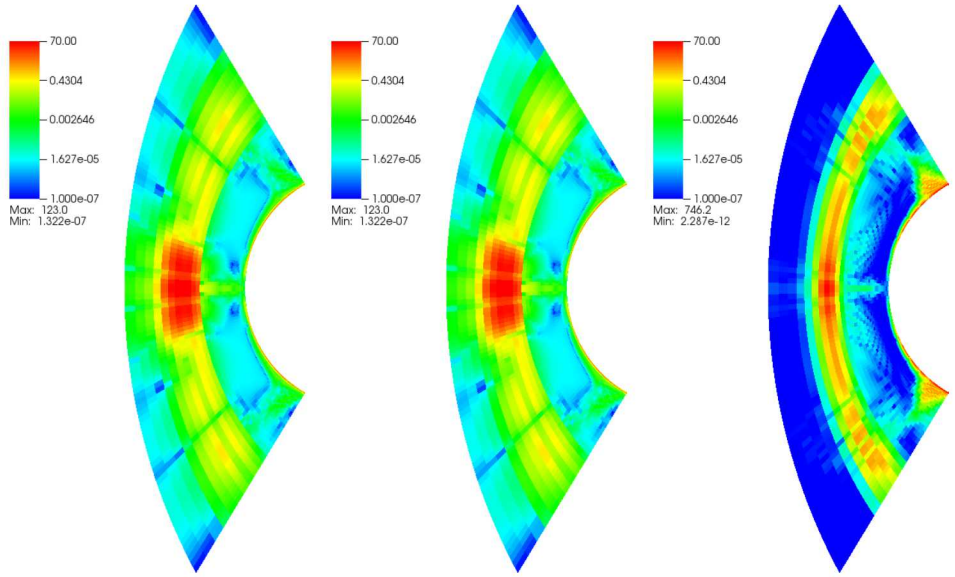

(a) P1 (b) P2 (c) P3

Fig. 2.20: Error indicator on Grid 2 for integrated surface heat flux using $Q1$ quadrilateral grids

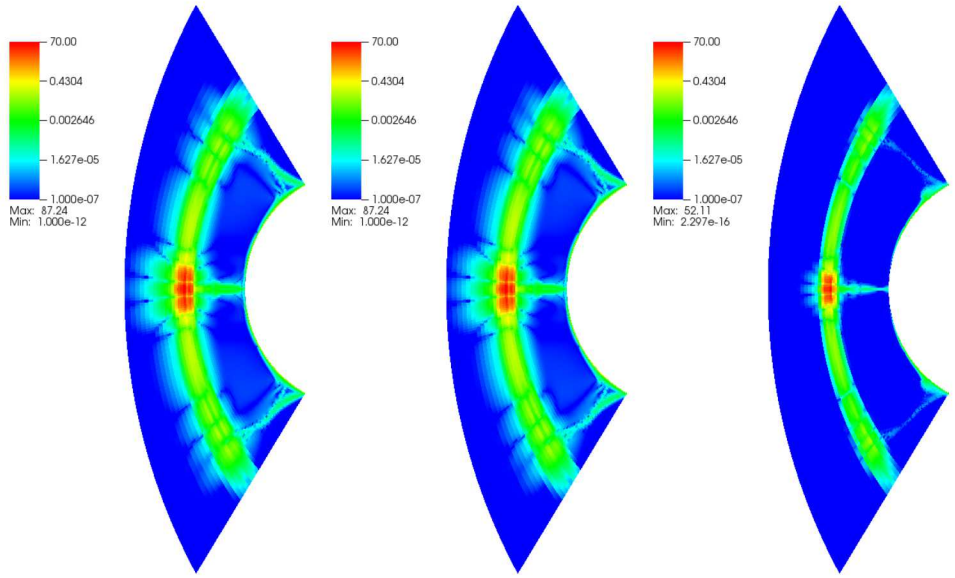

(a) P1 (b) P2 (c) P3

Fig. 2.21: Error indicator on Grid 3 for integrated surface heat flux using $Q1$ quadrilateral grids

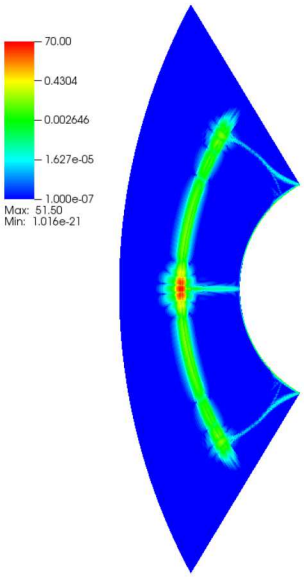

(a) P1

Fig. 2.22: Error indicator on Grid 4 for integrated surface heat flux using $Q1$ quadrilateral grids

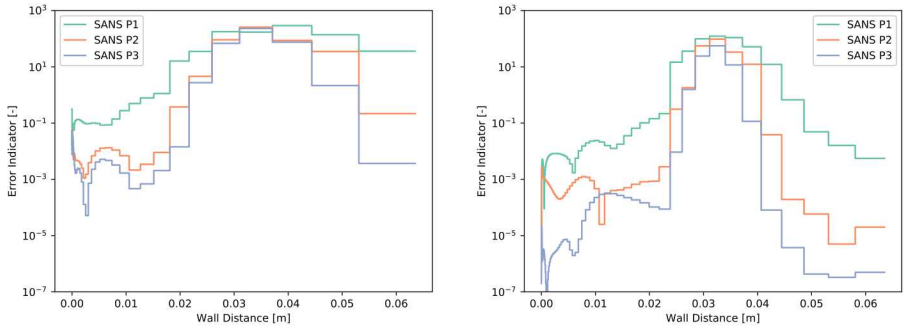

(a) Grid 1

(b) Grid 2

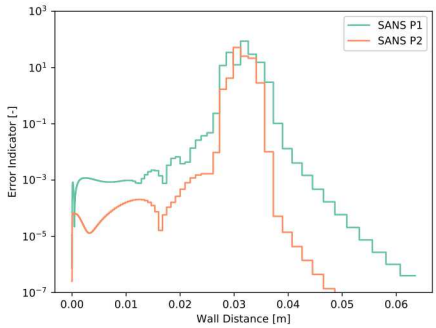

(c) Grid 3

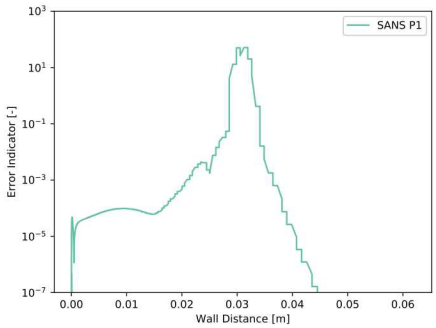

(d) Grid 4

Fig. 2.23: Error indicator along stagnation line of provided $Q1$ quadrilateral grids

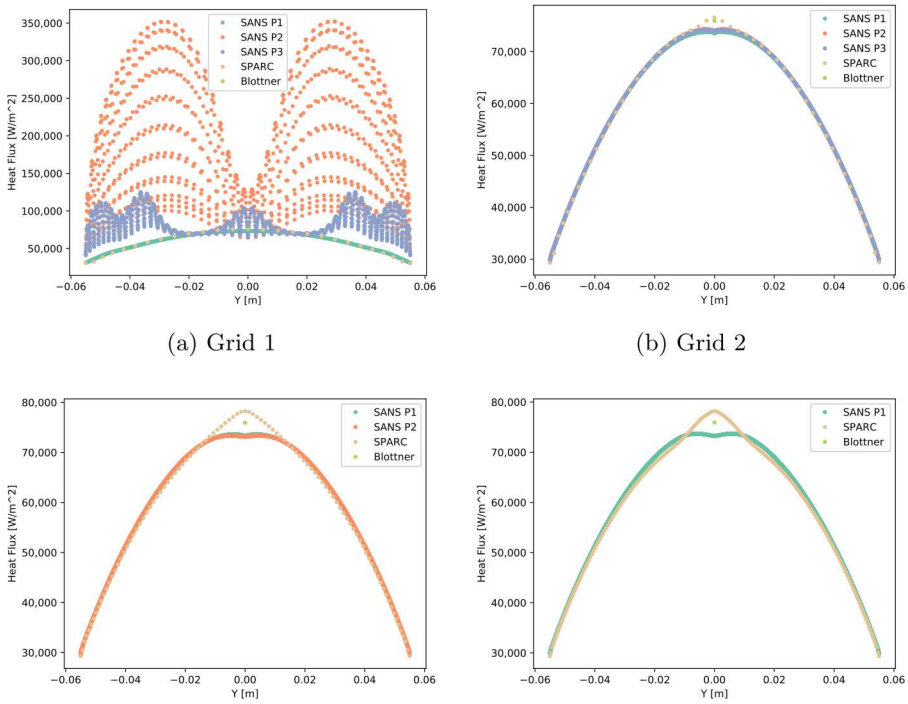

(a) Grid 1

(b) Grid 2

(c) Grid 3

(d) Grid 4

Fig. 2.24: Heat flux predicted using provided $Q3$ quadrilateral grids

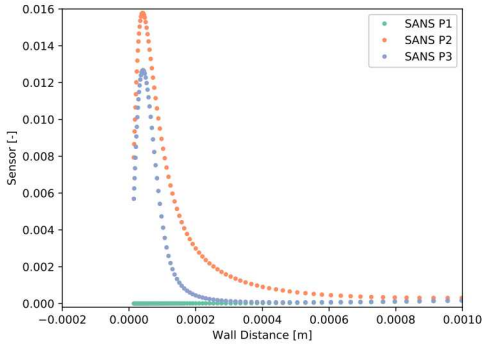

Fig. 2.25: Sensor along stagnation line for Grid 1

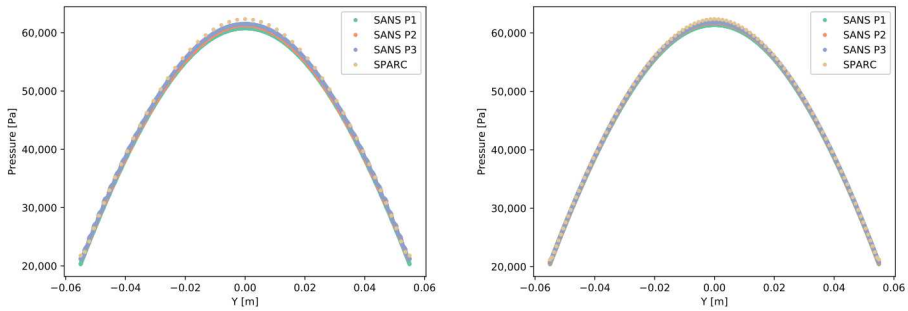

(a) Grid 1

(b) Grid 2

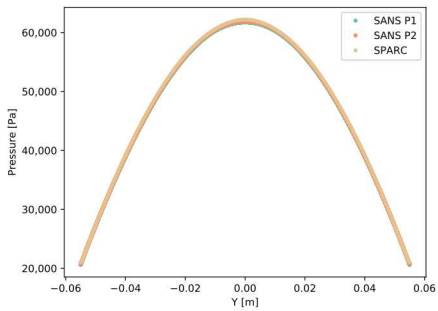

(c) Grid 3

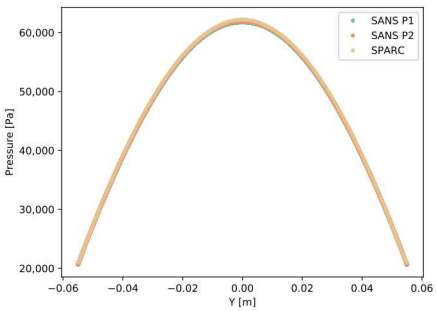

(d) Grid 4

Fig. 2.26: Surface pressure predicted using provided $Q3$ quadrilateral grids

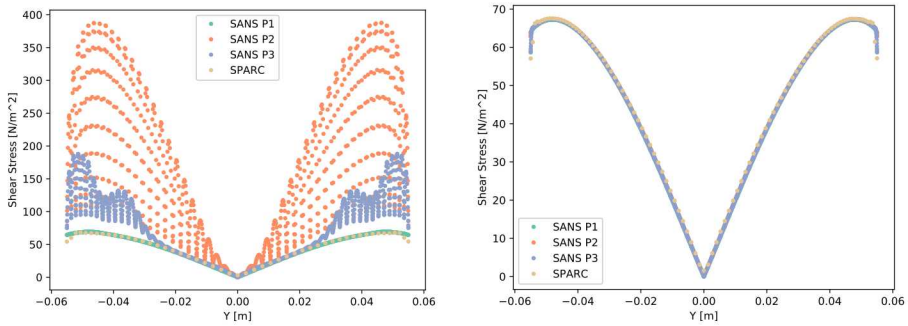

(a) Grid 1

(b) Grid 2

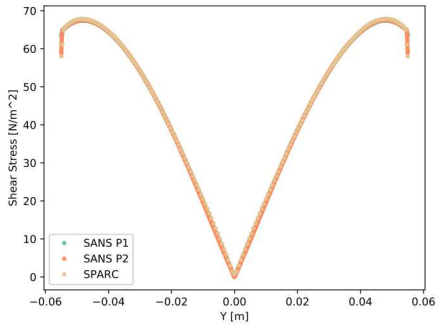

(c) Grid 3

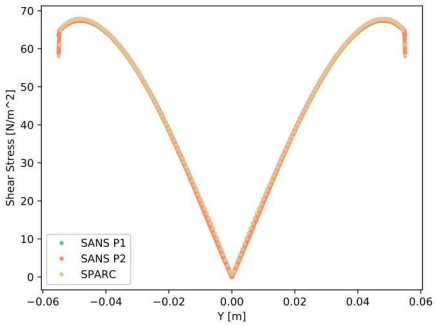

(d) Grid 4

Fig. 2.27: Surface shear predicted using provided $Q3$ quadrilateral grids

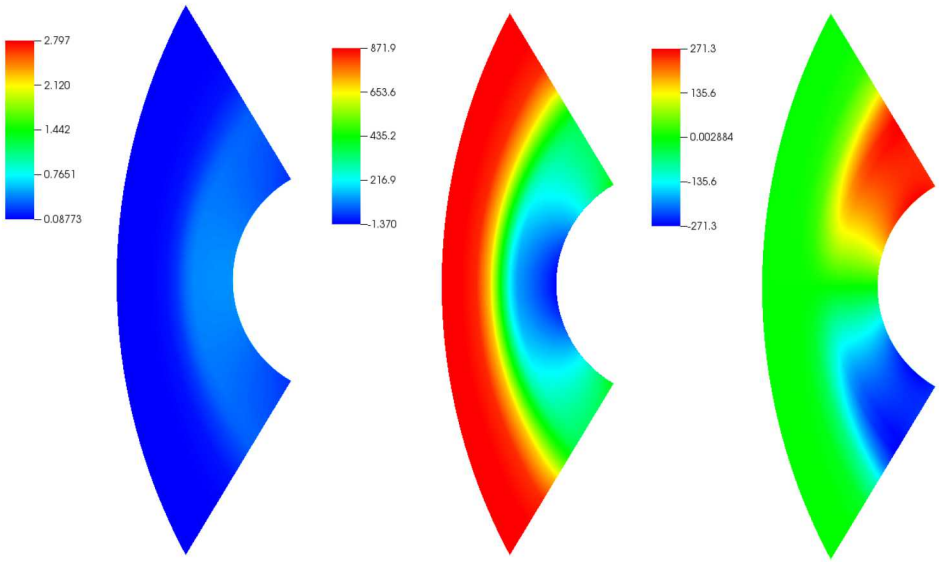

(a) Density (b) X-Velocity (c) Y-Velocity

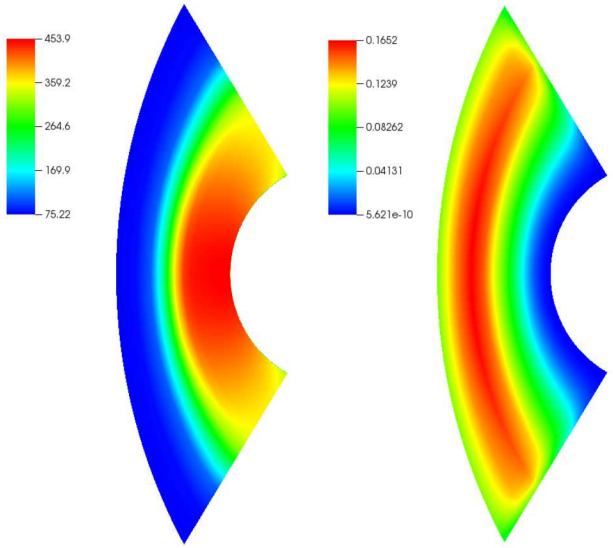

(d) Temperature (e) Sensor

Fig. 2.28: Primal P1 solution on $Q3$ Grid 1

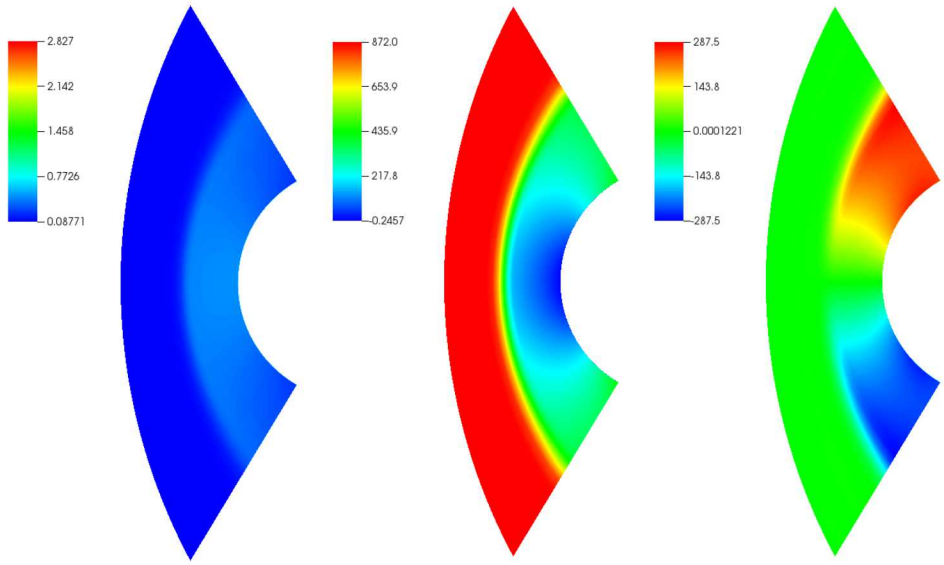

(a) Density (b) X-Velocity (c) Y-Velocity

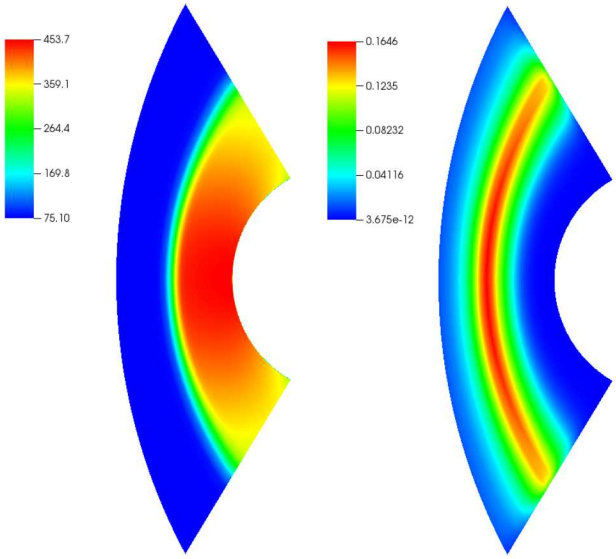

(d) Temperature (e) Sensor

Fig. 2.29: Primal P1 solution on $Q3$ Grid 2

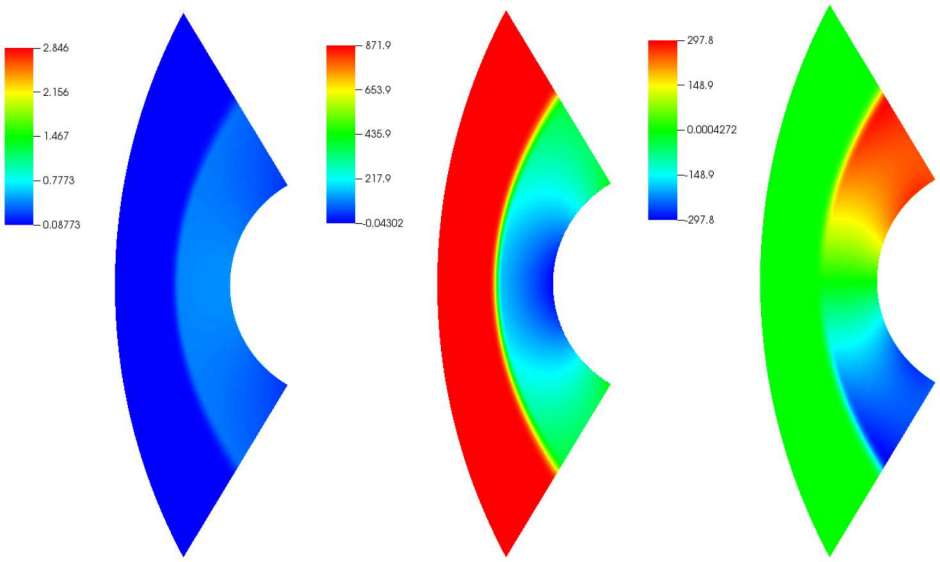

(a) Density (b) X-Velocity (c) Y-Velocity

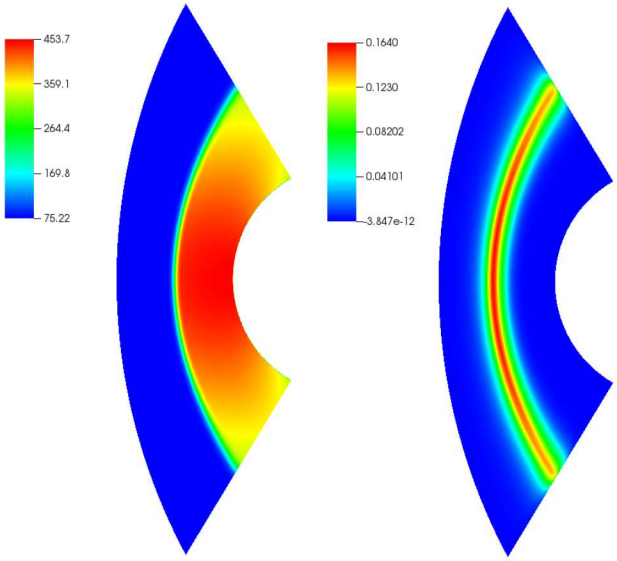

(d) Temperature (e) Sensor

Fig. 2.30: Primal P1 solution on $Q3$ Grid 3

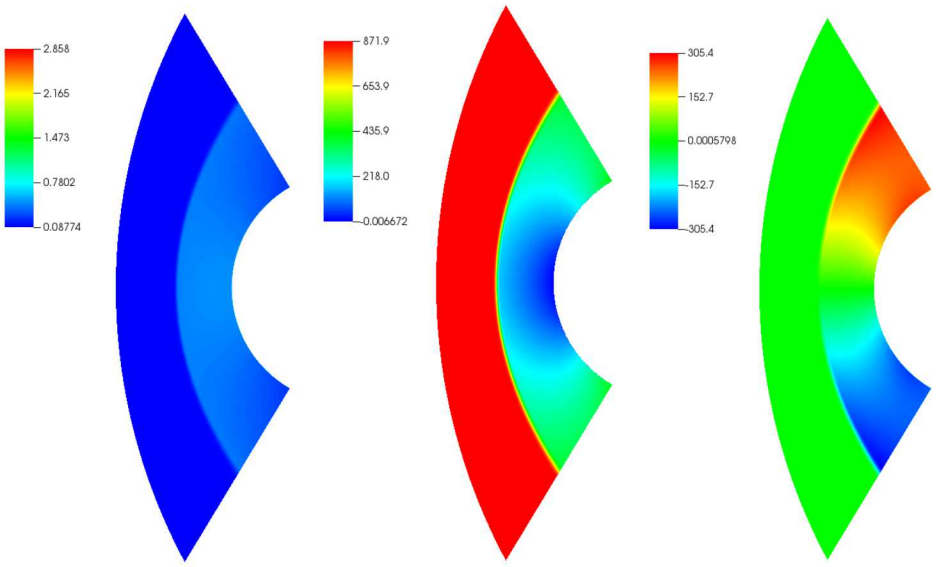

(a) Density (b) X-Velocity (c) Y-Velocity

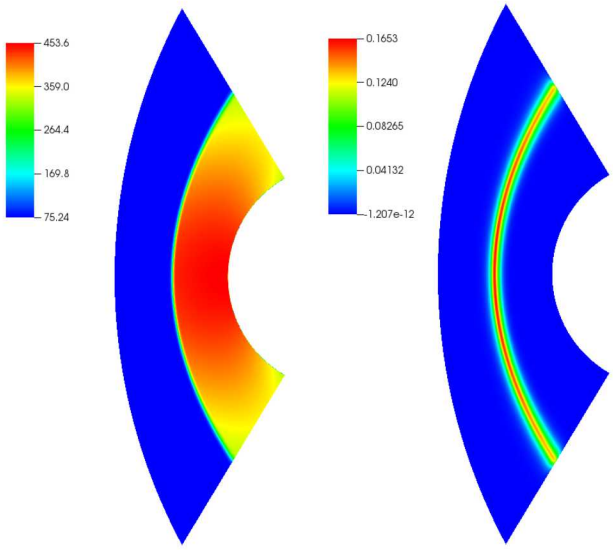

(d) Temperature (e) Sensor

Fig. 2.31: Primal P1 solution on $Q3$ Grid 4

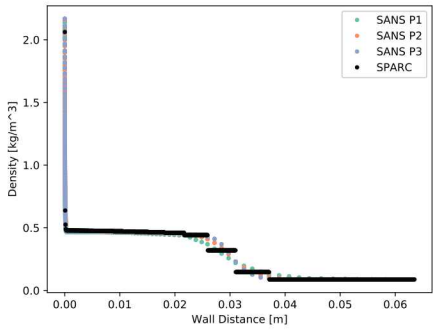

(a) Stagnation streamline to computational domain boundary

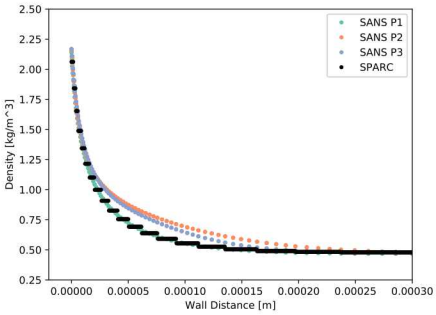

(b) Stagnation streamline focus on boundary layer

Fig. 2.32: Stagnation streamline density profiles on Grid 1

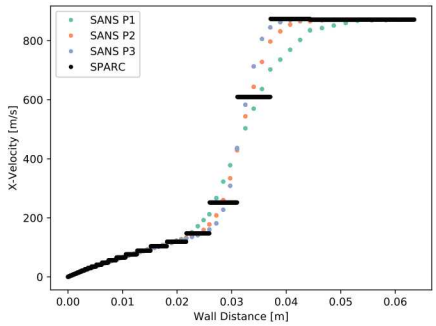

(a) Stagnation streamline to computational domain boundary

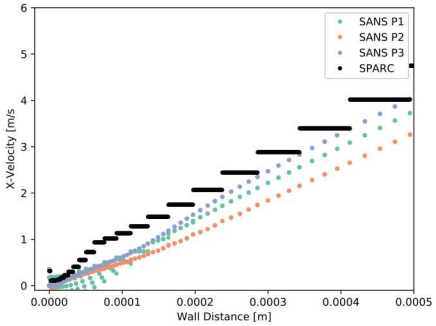

(b) Stagnation streamline focus on boundary layer

Fig. 2.33: Stagnation streamline velocity profiles on Grid 1

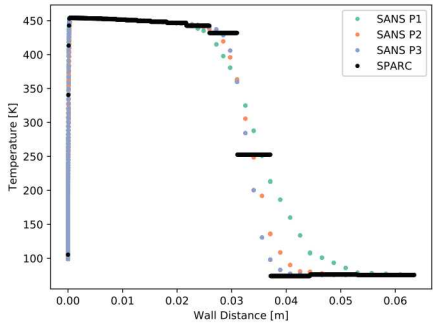

(a) Stagnation streamline to computational domain boundary

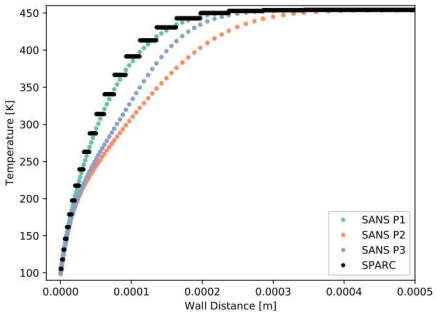

(b) Stagnation streamline focus on boundary layer

Fig. 2.34: Stagnation streamline temperature profiles on Grid 1

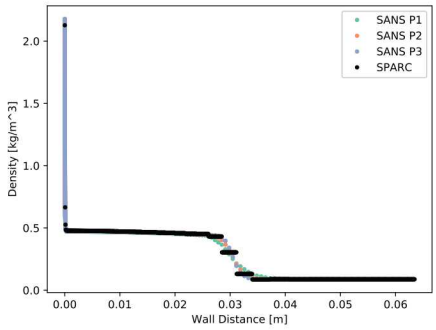

(a) Stagnation streamline to computational domain boundary

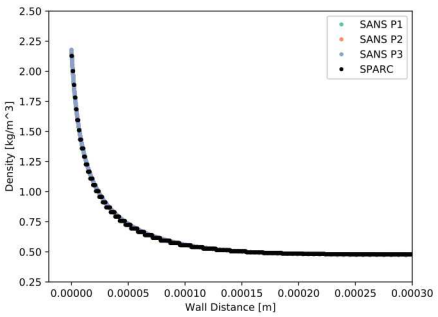

(b) Stagnation streamline focus on boundary layer

Fig. 2.35: Stagnation streamline density profiles on Grid 2

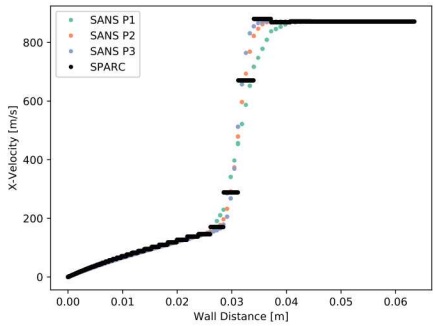

(a) Stagnation streamline to computational domain boundary

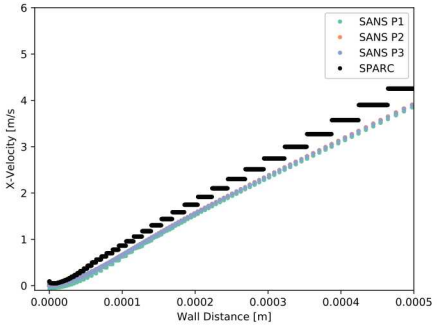

(b) Stagnation streamline focus on boundary layer

Fig. 2.36: Stagnation streamline velocity profiles on Grid 2

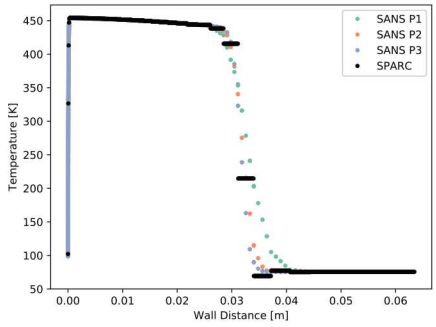

(a) Stagnation streamline to computational domain boundary

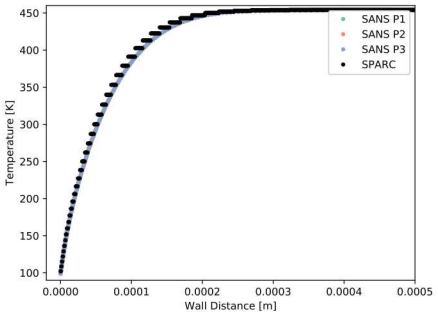

(b) Stagnation streamline focus on boundary layer

Fig. 2.37: Stagnation streamline temperature profiles on Grid 2

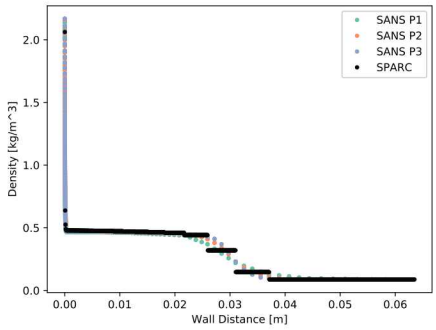

(a) Stagnation streamline to computational domain boundary

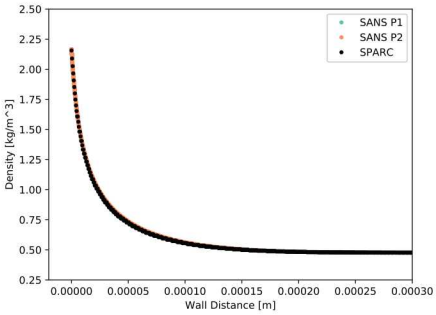

(b) Stagnation streamline focus on boundary layer

Fig. 2.38: Stagnation streamline density profiles on Grid 3

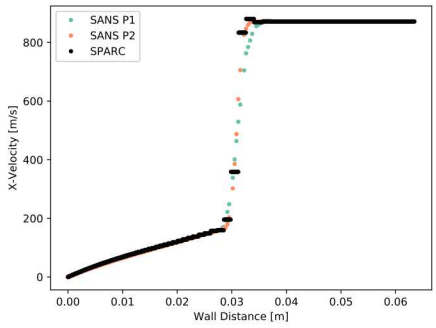

(a) Stagnation streamline to computational domain boundary

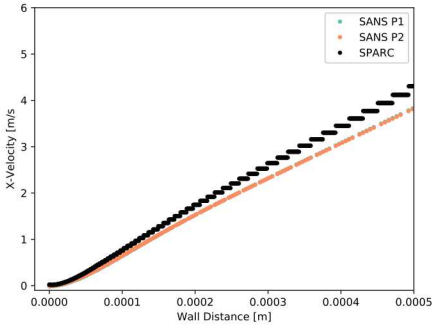

(b) Stagnation streamline focus on boundary layer

Fig. 2.39: Stagnation streamline velocity profiles on Grid 3

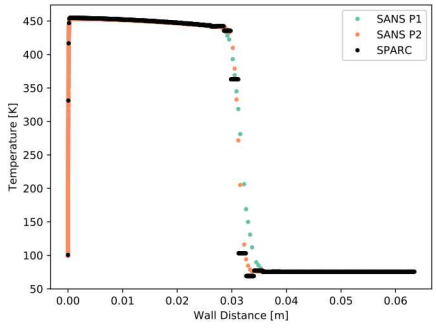

(a) Stagnation streamline to computational domain boundary

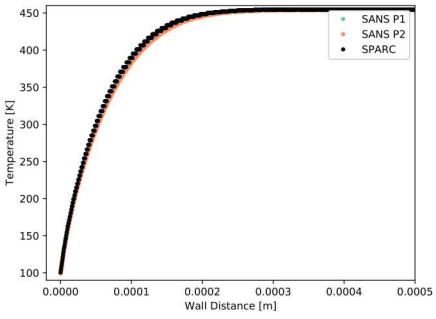

(b) Stagnation streamline focus on boundary layer

Fig. 2.40: Stagnation streamline temperature profiles on Grid 3

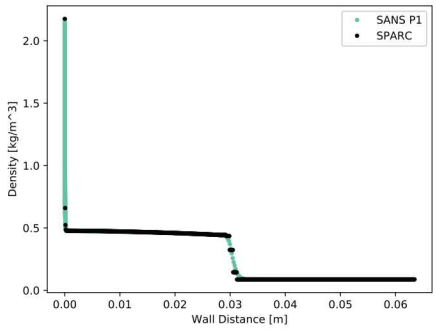

(a) Stagnation streamline to computational domain boundary

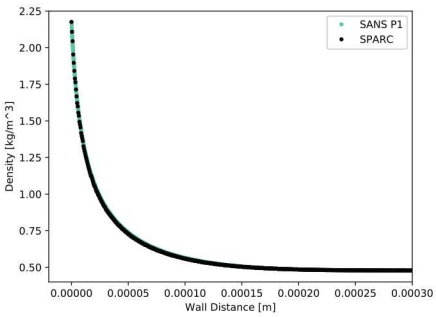

(b) Stagnation streamline focus on boundary layer

Fig. 2.41: Stagnation streamline density profiles on Grid 4

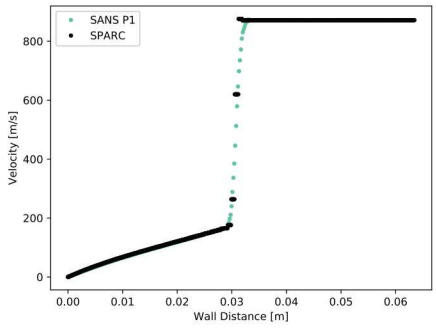

(a) Stagnation streamline to computational domain boundary

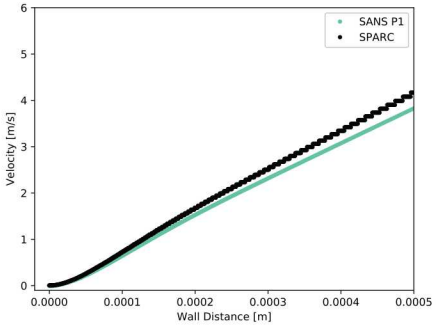

(b) Stagnation streamline focus on boundary layer

Fig. 2.42: Stagnation streamline velocity profiles on Grid 4

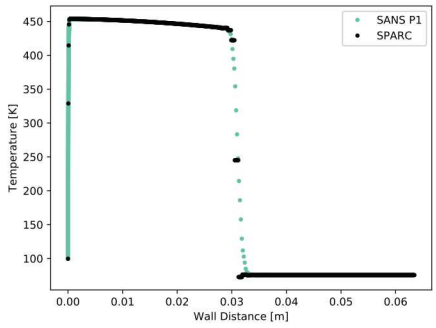

(a) Stagnation streamline to computational domain boundary

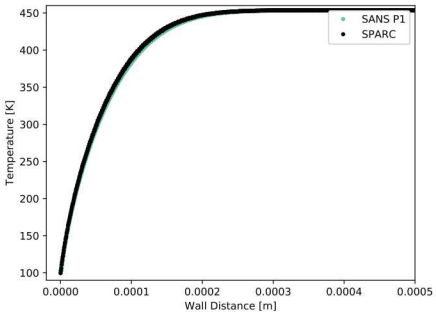

(b) Stagnation streamline focus on boundary layer

Fig. 2.43: Stagnation streamline temperature profiles on Grid 4

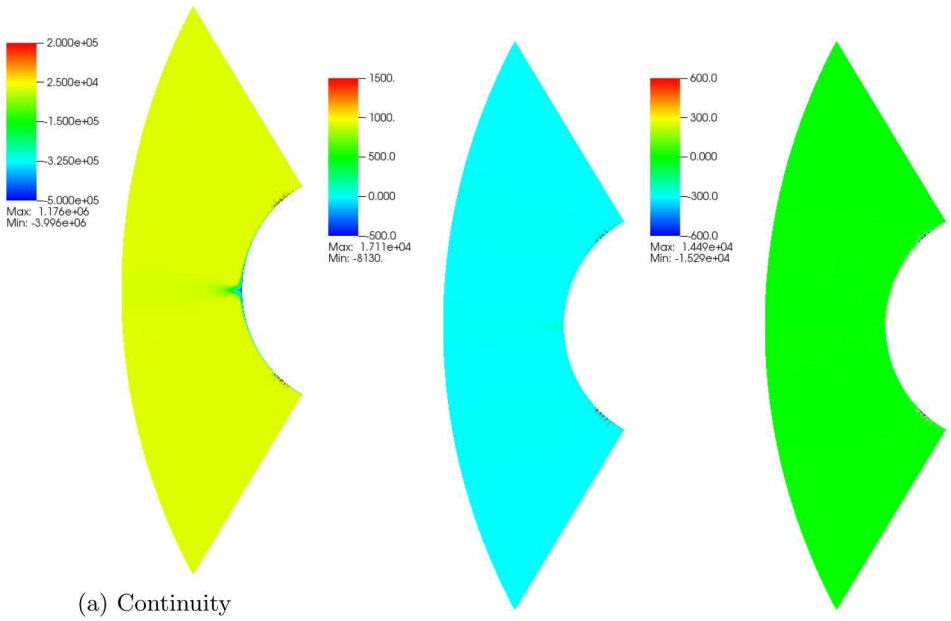

(a) Continuity (b) X-momentum (c) Y-momentum

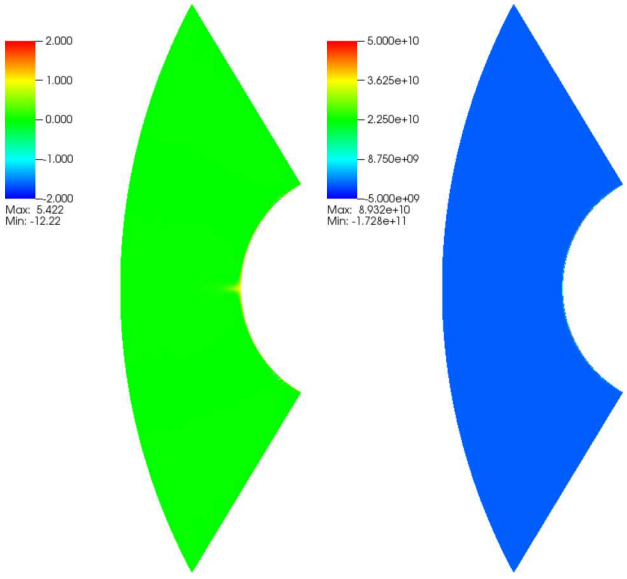

(d) Total internal energy (e) Sensor

Fig. 2.44: Adjoint P1 solution on $Q3$ Grid 1

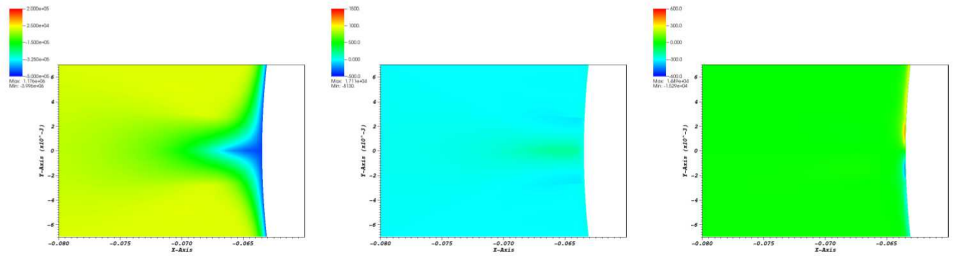

(a) Continuity (b) X-momentum (c) Y-momentum

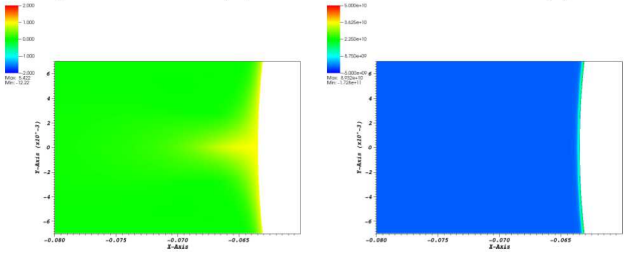

(d) Total internal energy (e) Sensor

Fig. 2.45: Adjoint P1 solution on $Q3$ Grid 1, focus on stagnation point

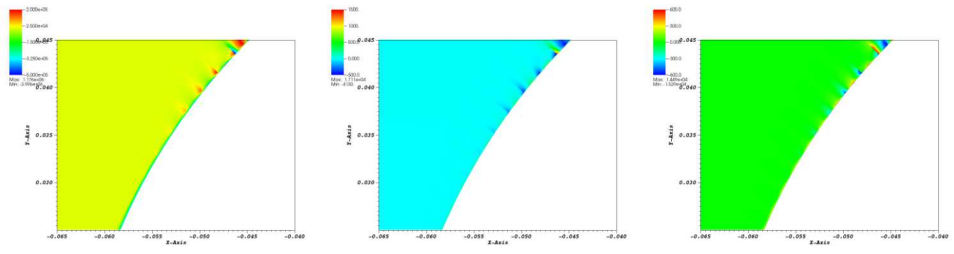

(a) Continuity (b) X-momentum (c) Y-momentum

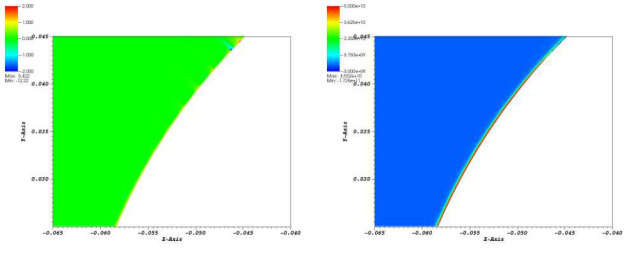

(d) Total internal energy (e) Sensor

Fig. 2.46: Adjoint P1 solution on $Q3$ Grid 1, focus on surface half way around computational domain

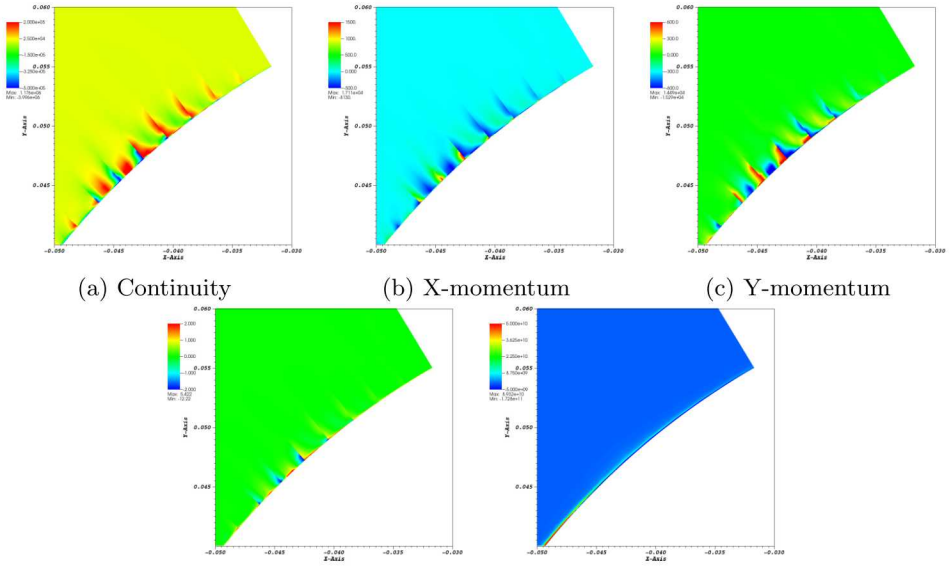

(a) Continuity (b) X-momentum (c) Y-momentum

(d) Total internal energy (e) Sensor

Fig. 2.47: Adjoint P1 solution on $Q3$ Grid 1, focus on surface at edge of computational domain

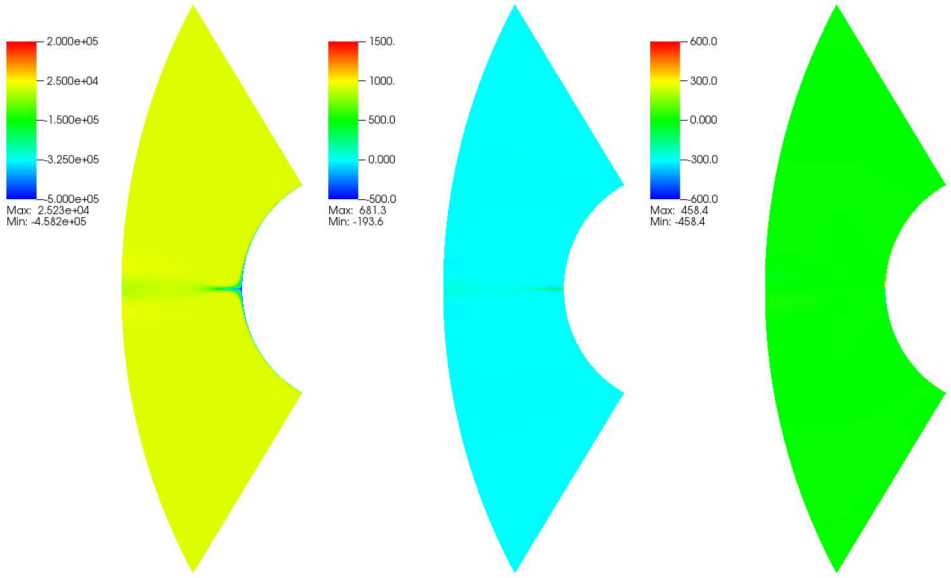

(a) Continuity (b) X-momentum (c) Y-momentum

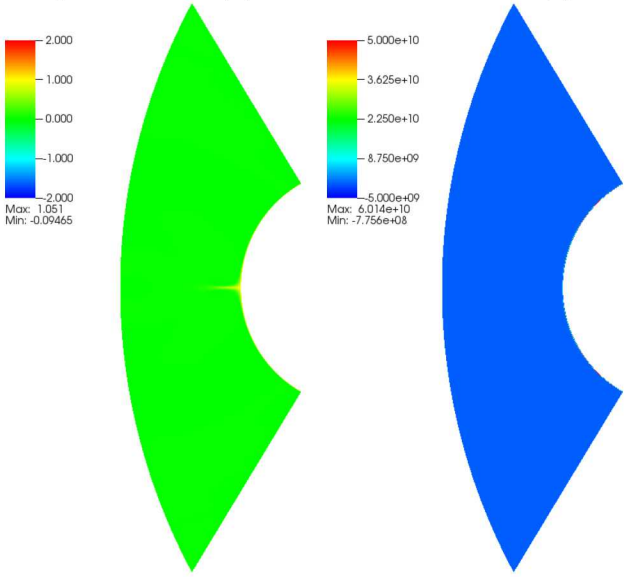

(d) Total internal energy (e) Sensor

Fig. 2.48: Adjoint P1 solution on $Q3$ Grid 2

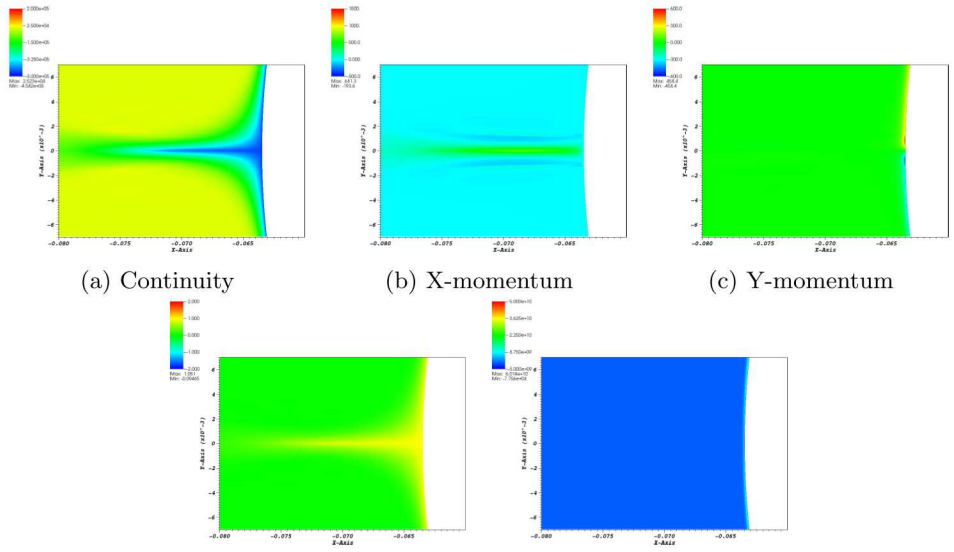

(a) Continuity (b) X-momentum (c) Y-momentum

(d) Total internal energy (e) Sensor

Fig. 2.49: Adjoint P1 solution on $Q3$ Grid 2, focus on stagnation point

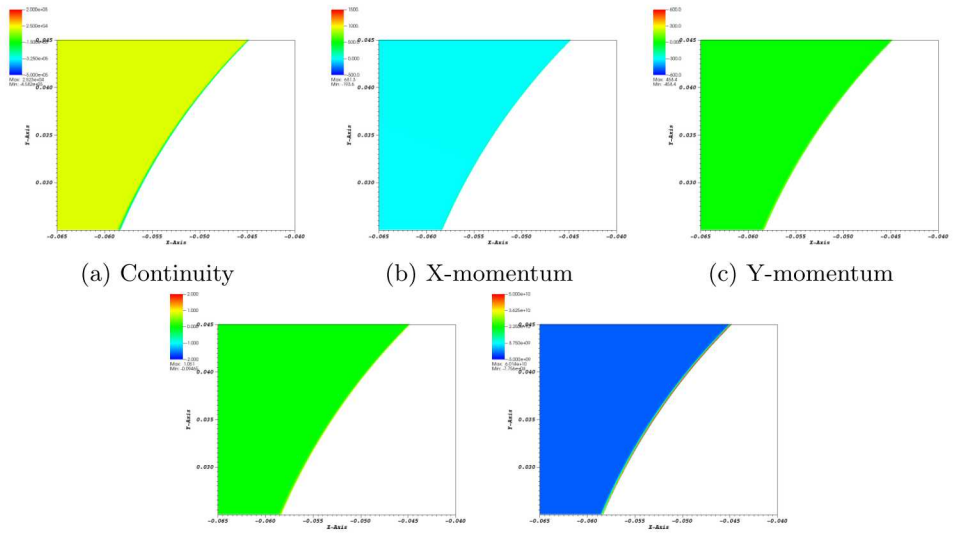

(a) Continuity (b) X-momentum (c) Y-momentum

(d) Total internal energy (e) Sensor

Fig. 2.50: Adjoint P1 solution on $Q3$ Grid 2, focus on surface half way around computational domain

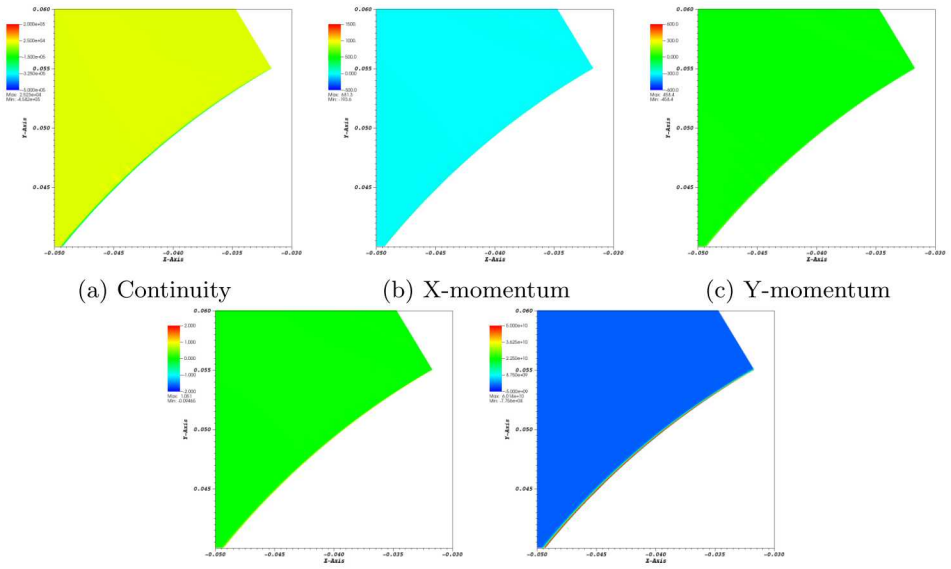

(a) Continuity (b) X-momentum (c) Y-momentum

(d) Total internal energy (e) Sensor

Fig. 2.51: Adjoint P1 solution on $Q3$ Grid 2, focus on surface at edge of computational domain

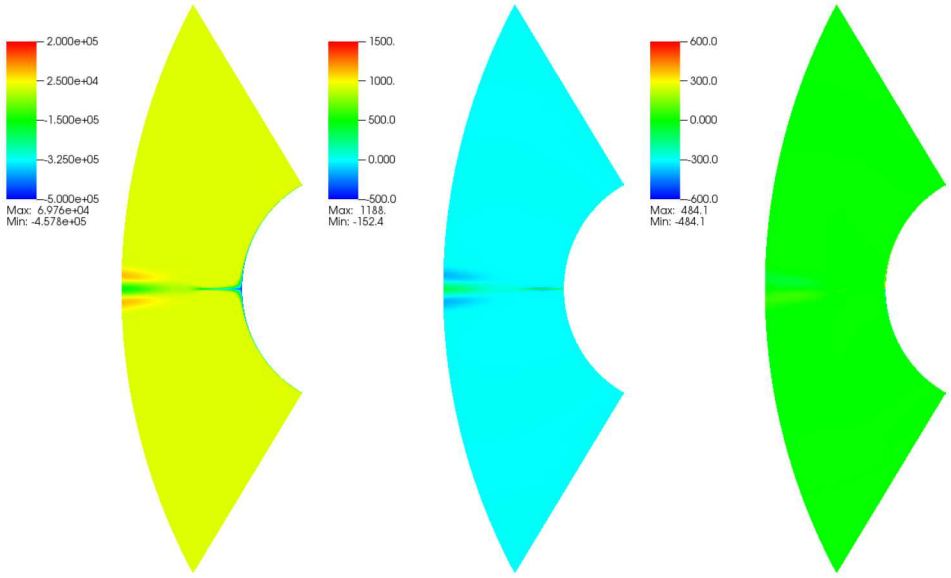

(a) Continuity (b) X-momentum (c) Y-momentum

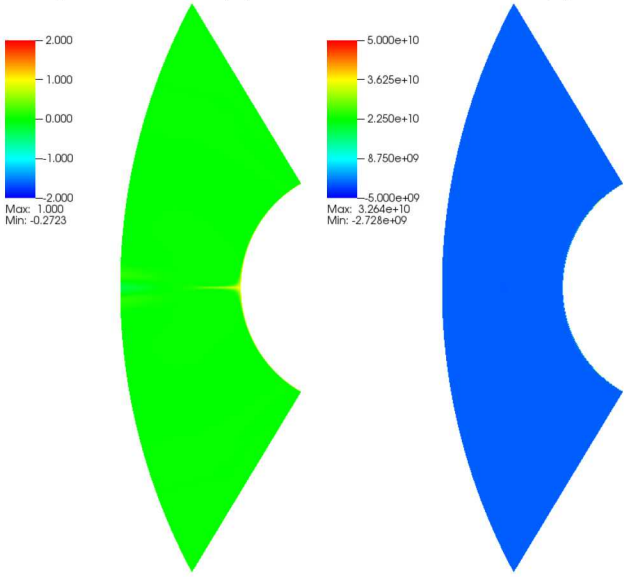

(d) Total internal energy (e) Sensor

Fig. 2.52: Adjoint P1 solution on $Q3$ Grid 3

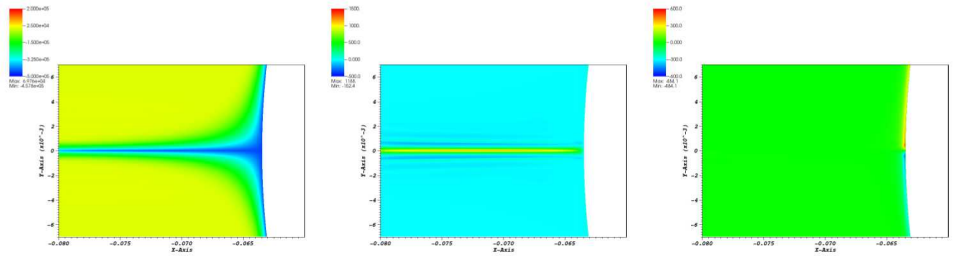

(a) Continuity (b) X-momentum (c) Y-momentum

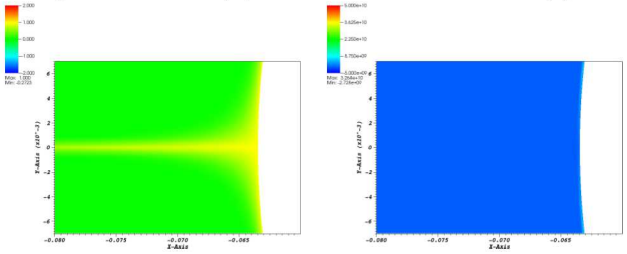

(d) Total internal energy (e) Sensor

Fig. 2.53: Adjoint P1 solution on $Q3$ Grid 3, focus on stagnation point

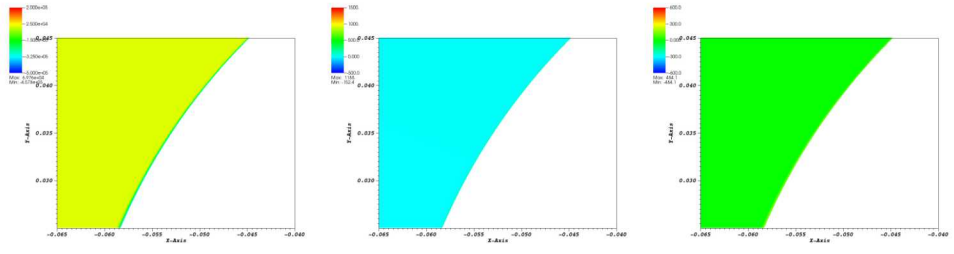

(a) Continuity (b) X-momentum (c) Y-momentum

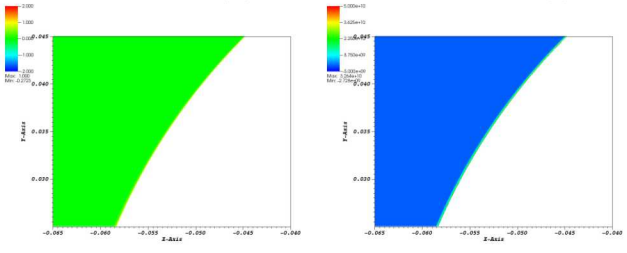

(d) Total internal energy (e) Sensor

Fig. 2.54: Adjoint P1 solution on $Q3$ Grid 3, focus on surface half way around computational domain

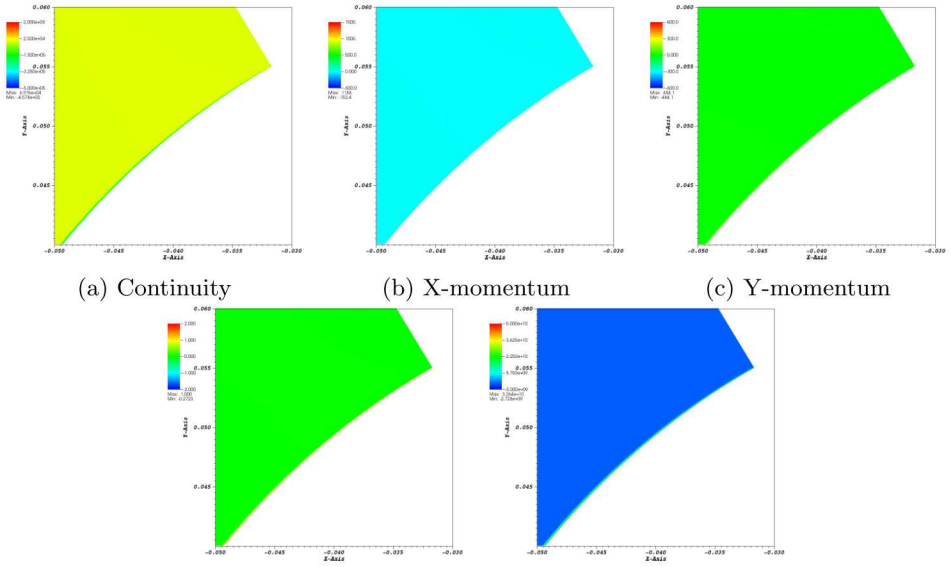

(a) Continuity (b) X-momentum (c) Y-momentum

(d) Total internal energy (e) Sensor

Fig. 2.55: Adjoint P1 solution on $Q3$ Grid 3, focus on surface at edge of computational domain

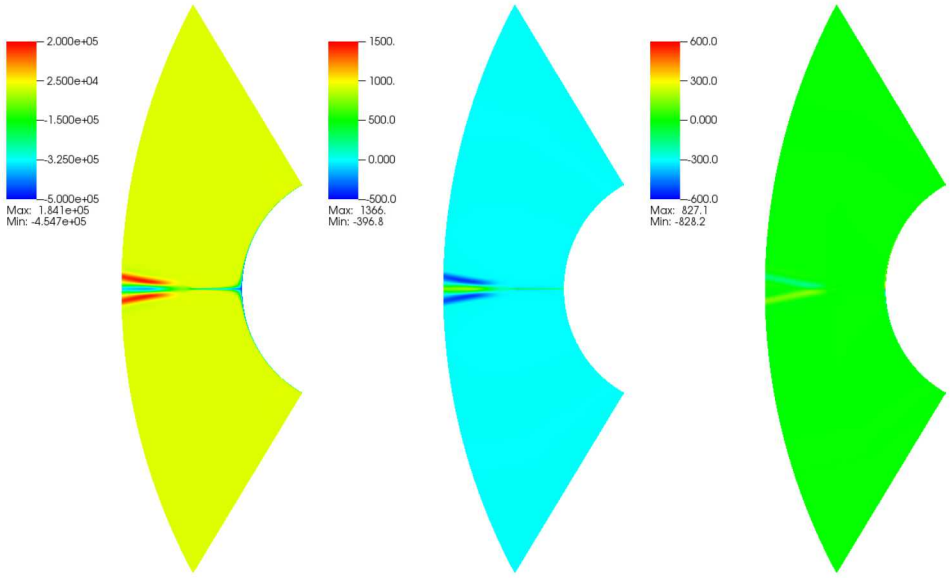

(a) Continuity (b) X-momentum (c) Y-momentum

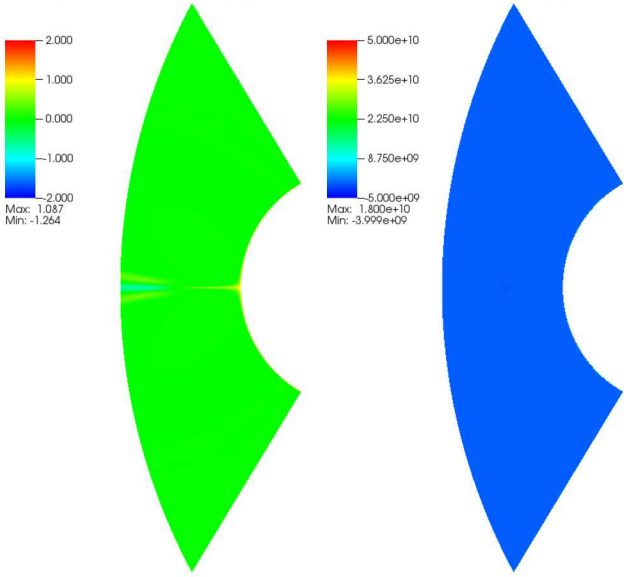

(d) Total internal energy (e) Sensor

Fig. 2.56: Adjoint P1 solution on $Q3$ Grid 4

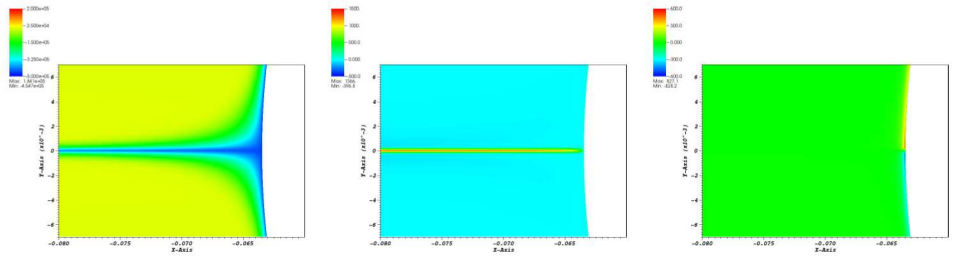

(a) Continuity (b) X-momentum (c) Y-momentum

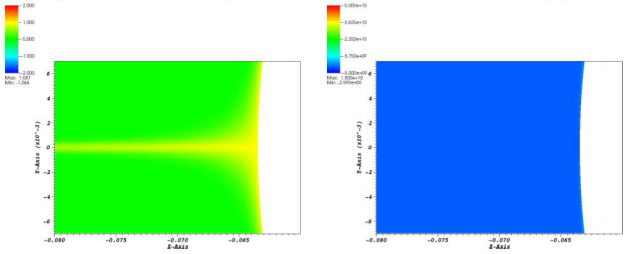

(d) Total internal energy (e) Sensor

Fig. 2.57: Adjoint P1 solution on $Q3$ Grid 4, focus on stagnation point

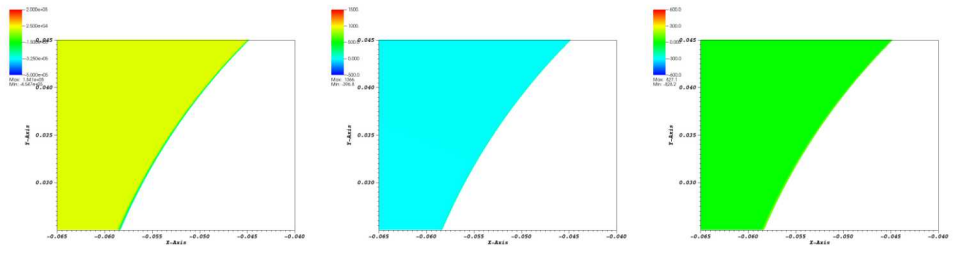

(a) Continuity (b) X-momentum (c) Y-momentum

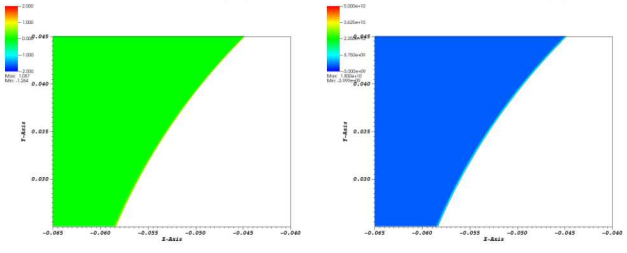

(d) Total internal energy (e) Sensor

Fig. 2.58: Adjoint P1 solution on $Q3$ Grid 4, focus on surface half way around computational domain

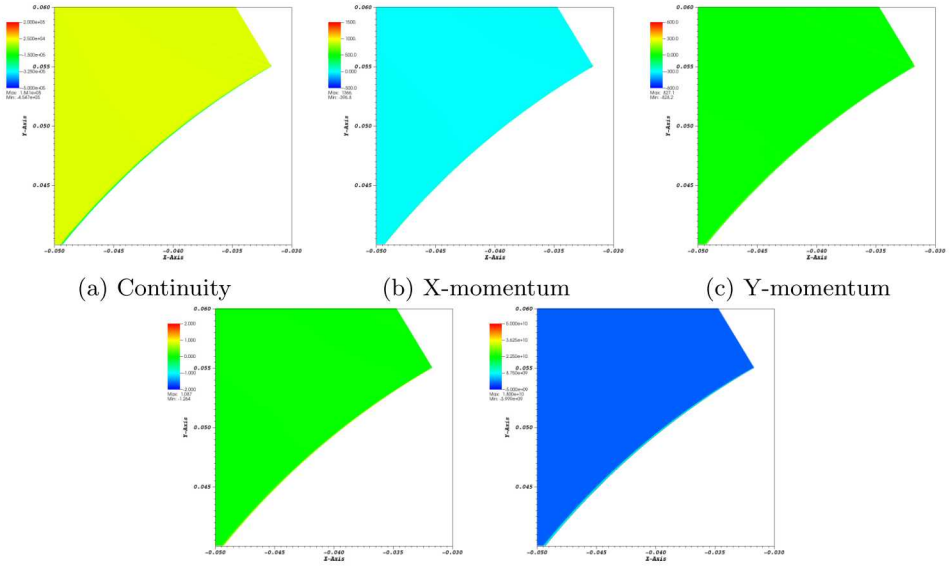

(a) Continuity (b) X-momentum (c) Y-momentum

(d) Total internal energy (e) Sensor

Fig. 2.59: Adjoint P1 solution on $Q3$ Grid 4, focus on surface at edge of computational domain

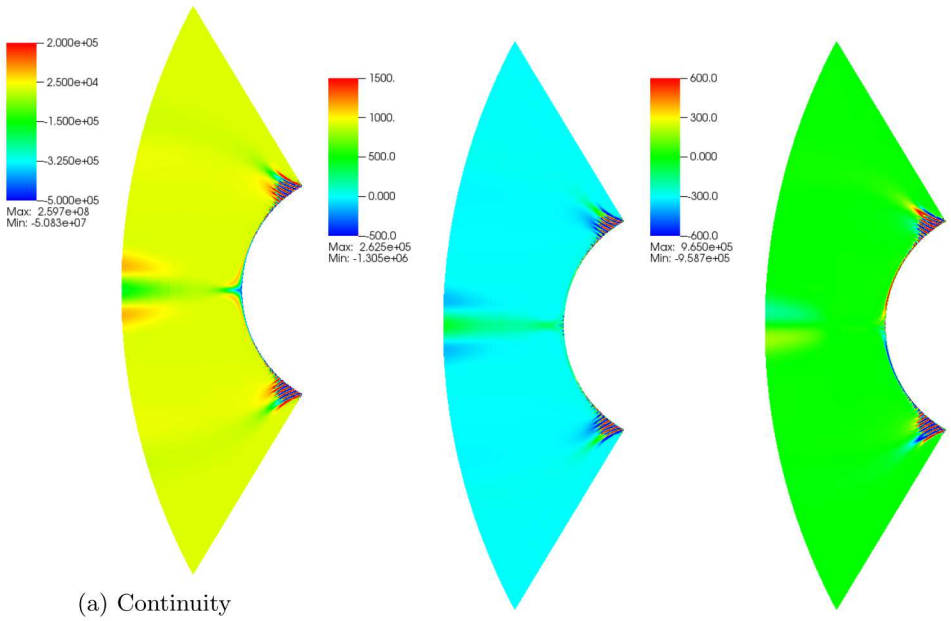

(a) Continuity

(b) X-momentum

(c) Y-momentum

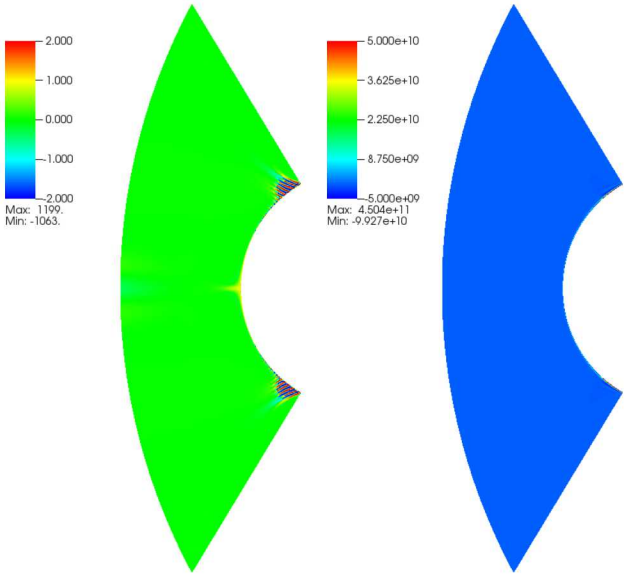

(d) Total internal energy

(e) Sensor

Fig. 2.60: Adjoint P3 solution on $Q3$ Grid 1

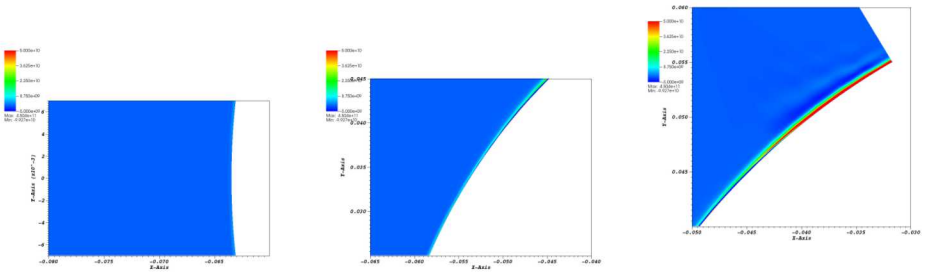

(a) Stagnition point (b) Mid-cylinder (c) Edge of compuational domain

Fig. 2.61: Sensor equation adjoint P3 solution on $Q3$ Grid 1

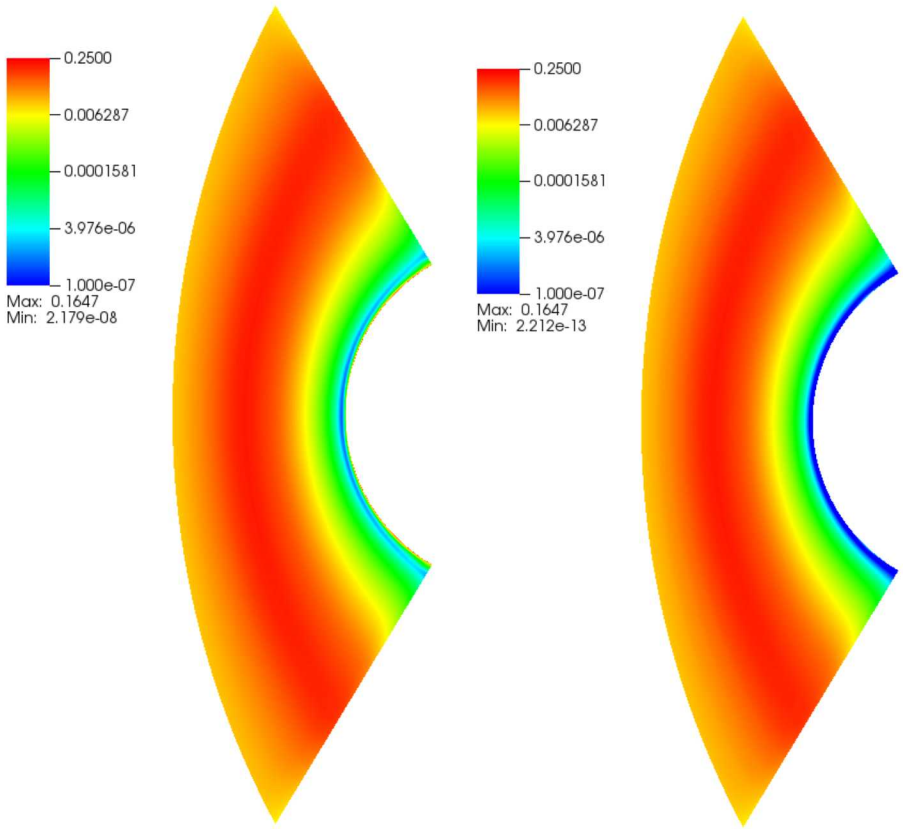

(a) $Q1$ Grid (b) $Q3$ Grid

Fig. 2.62: Sensor field for Grid 2 P1 solution

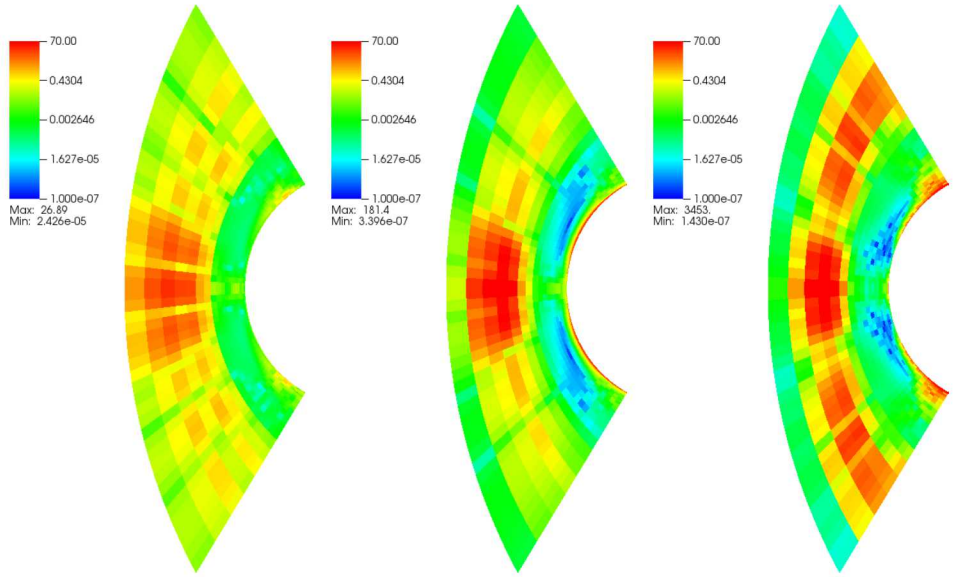

(a) P1 (b) P2 (c) P3

Fig. 2.63: Error indicator on Grid 1 for integrated surface heat flux using $Q3$ quadrilateral grids

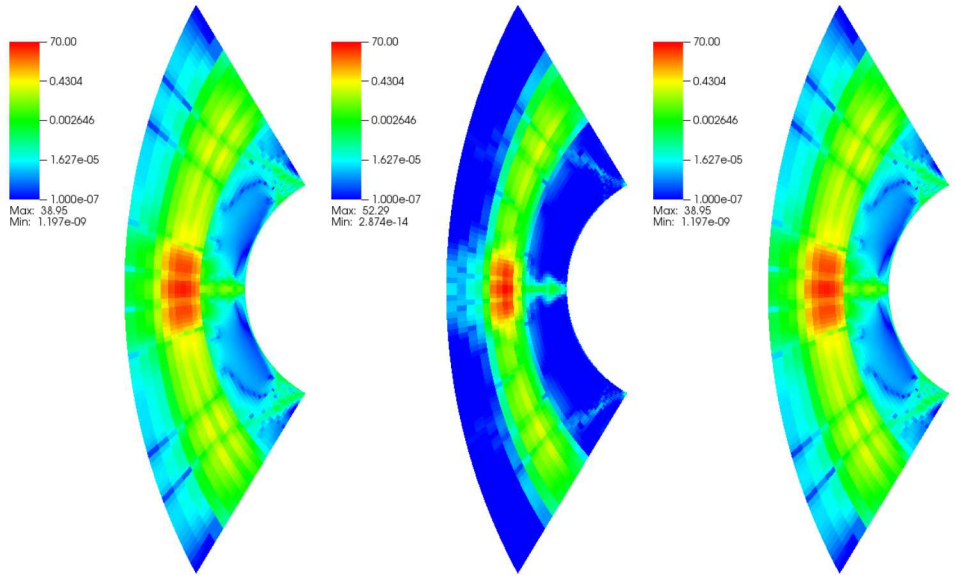

(a) P1 (b) P2 (c) P3

Fig. 2.64: Error indicator on Grid 2 for integrated surface heat flux using $Q3$ quadrilateral grids

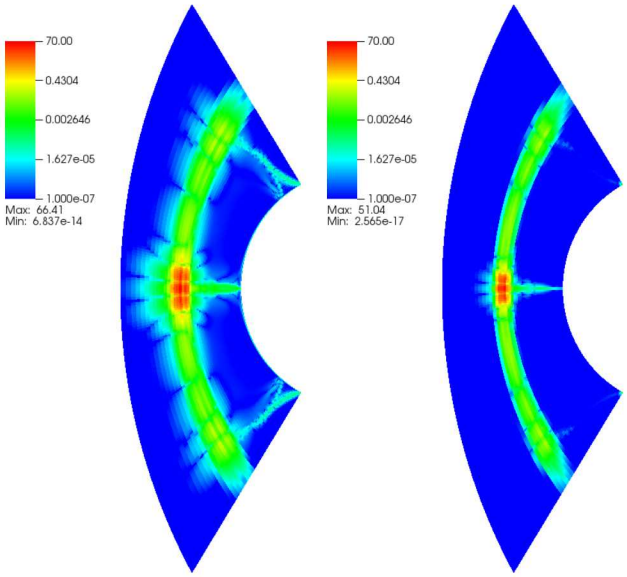

(a) P1 (b) P2

Fig. 2.65: Error indicator on Grid 3 for integrated surface heat flux using $Q3$ quadrilateral grids

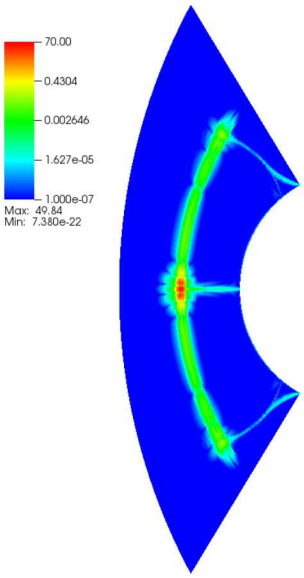

(a) P1

Fig. 2.66: Error indicator on Grid 4 for integrated surface heat flux using $Q3$ quadrilateral grids

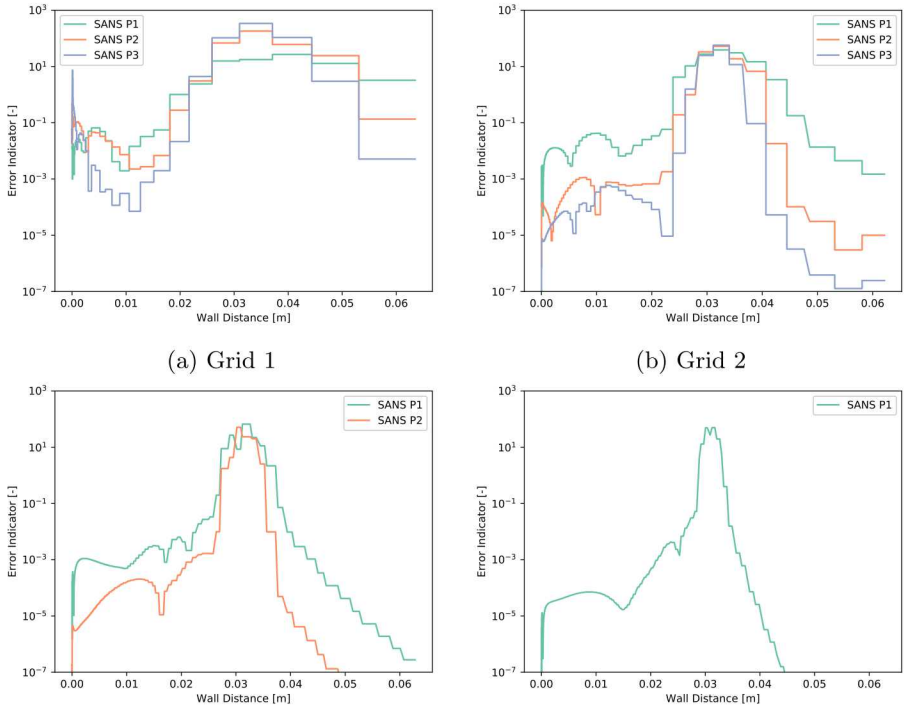

(a) Grid 1

(b) Grid 2

(c) Grid 3

(d) Grid 4

Fig. 2.67: Error indicator along stagnation line of provided $Q3$ quadrilateral grids

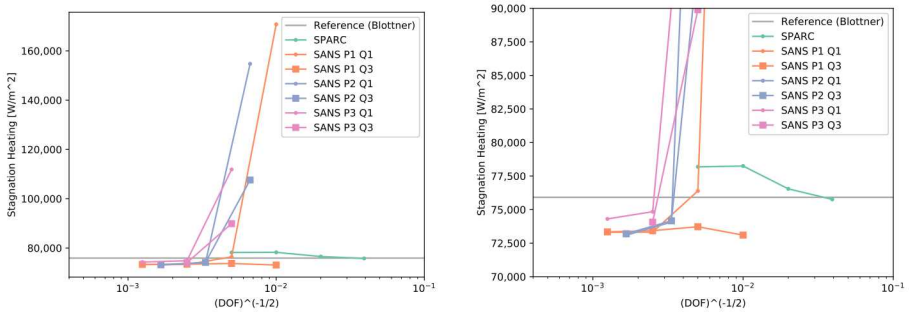

(a) All data

(b) Zoomed

Fig. 2.68: Stagnation heat flux predicted using provided quadrilateral grids

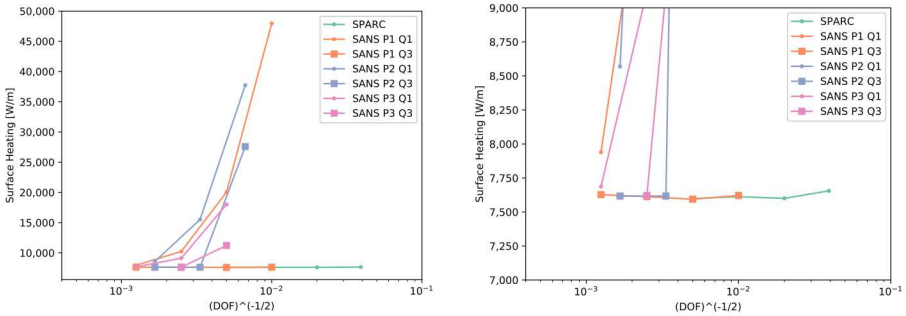

(a) All data (b) Zoomed

Fig. 2.69: Surface integrated heat flux predicted using provided quadrilateral grids

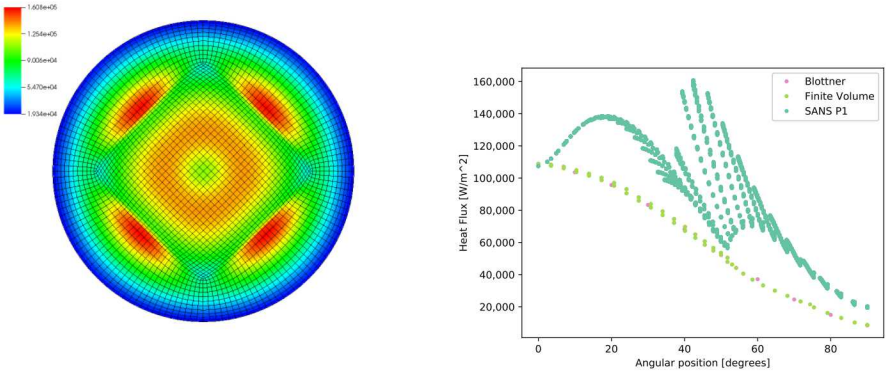

(a) $3D$ heat flux profile – looking along freestream velocity vector

(b) Angular heat flux profiles overe sphere surface

Fig. 3.1: Heat flux over sphere using $Q1$ grid

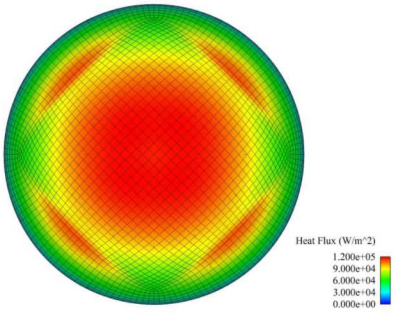

Fig. 3.2: Heat flux over the Blottner Sphere, as predicted by Kirk et al.[7]

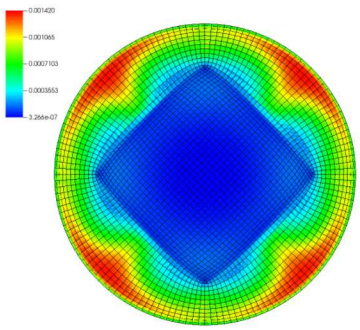

Fig. 3.3: Surface artificial viscosity (ϵ_{xx}) profile – looking along freestream velocity vector

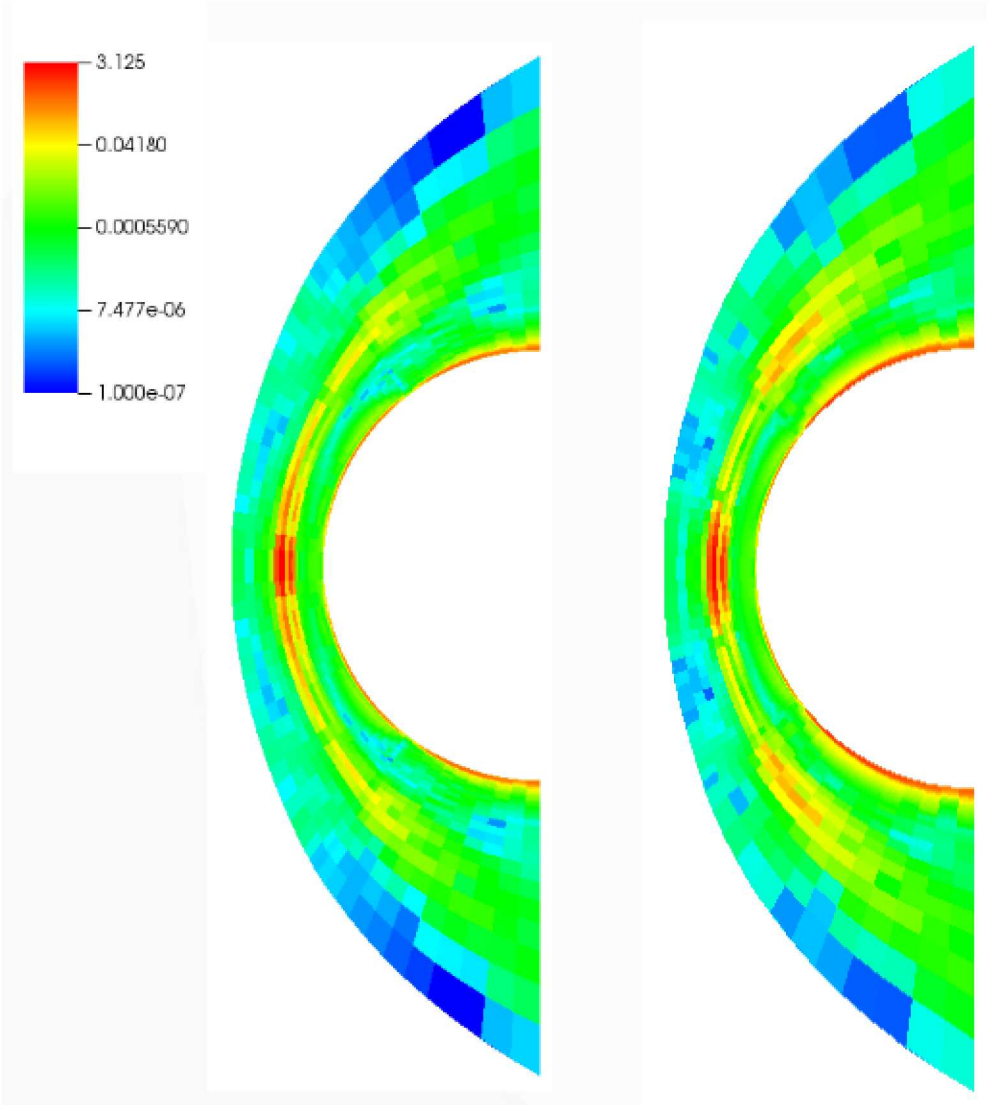

Fig. 3.4: Error indicator slices for $Q1$ sphere grid

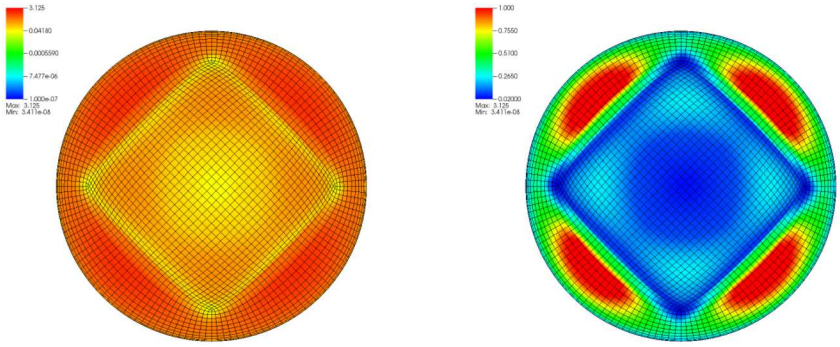

(a) Log scale (b) LinearScale

Fig. 3.5: Error indicator over surface of $Q1$ sphere grid result